Ore Geology Reviews 127 (2020) 103757

Contents lists available at ScienceDirect

Ore Geology Reviews

journal homepage: www.elsevier.com/locate/oregeorev

Evaluating magmatic fertility of Paleo-Tethyan granitoids in eastern Tibet using apatite chemical composition and Nd isotope

Li-Chuan Pan[a,*], Rui-Zhong Hu[a,b], Xian-Wu Bi[a], Yong Wang[c], Jun Yan[a]

[a] State Key Laboratory of Ore Deposit Geochemistry, Institute of Geochemistry, Chinese Academy of Sciences, Guiyang 550081, China
[b] College of Earth and Planetary Sciences, University of Chinese Academy of Sciences, Beijing 100049, China
[c] The Bureau of Geology and 108 Mineral Exploration Team of Sichuan Province, Chengdu 611200, China

ARTICLE INFO

Keywords:
Apatite
Granitoid
Porphyry Cu deposit
Magmatic fertility
Oxidation state
Paleo-Tethys Ocean

ABSTRACT

The Paleo-Tethyan granitoids in eastern Tibet are generally Cu-barren, and only a few can generate porphyry Cu deposits. It is still unclear what magmatic differences cause these coeval granitoids to have different mineralization potentials. In this study, the major, minor, and trace element abundances and Nd isotope in the apatites from four Triassic granitoids from eastern Tibet have been determined using EPMA, LA-ICP-MS, and LA-MC-ICP-MS. The following are the selected plutons: the Pulang pluton, which is associated with the porphyry-type Cu deposit, and the coeval Cuojiaoma, Dongcuo, and Daocheng plutons, three of which do not generate any Cu mineralization. Our study reveals that Ga, Ce, S, Cl, and Cu in apatite are effective indicators for both magmatic oxidation states and the abundances of volatiles and ore-forming metals. The Nd isotope of apatite can be used to trace the magma source. According to the above chemical compositions of apatite and Ce^{4+}/Ce^{3+} ratio of zircon, the parental magma of the Pulang pluton is identified to be more fertile for Cu mineralization than those of the other three plutons, i.e., Cuojiaoma, Dongcuo, and Daocheng, because it is more oxidized and richer in Cu, Cl, and S. The aforementioned differences in magmatic physical and chemical conditions among the plutons investigated are ascribed to the different sources and natures of magmas, as revealed by both the Nd isotope and δEu, Sr/Y, and La/Yb values of apatite. Generally, the results indicate that magmatic fertility mainly governs the Cu-mineralization potential of Paleo-Tethyan granitoids in eastern Tibet, and that apatite is a robust probe for magmatic fertility.

1. Introduction

Porphyry Cu deposits as a significant Cu source are accepted to mainly occur at the edge of the converging plate (Seedorf et al., 2005; Sillitoe, 2010). However, the subduction and collisional closure process of the Paleo-Tethys Ocean generated considerably sparse Cu deposits from the Alps to Indochina. The lack of Cu mineralization may be attributed to the widespread anoxia in the Paleo-Tethys Ocean basin, thereby resulting in the generation of relatively reduced arc magmas that were infertile for porphyry Cu formation (Richards and Şengör, 2017). However, some porphyry-type Cu deposits associated with Paleo-Tethyan subduction are generated in the eastern Tibet. It is not still understood whether these Cu-mineralized magmas are as reduced as the non-mineralized magmas, and which magmatic factors determine the Cu-mineralization potential of these granitoids. However, using traditional indicators of petrogeochemistry to identify magmatic chemical and physical conditions of granitoids is, sometimes, ineffective because rock samples associated with mineralization easily undergo weathering and alteration. Apatite ($Ca_5(PO_4)_3F$) is a common accessory phase in granitoid. It is insensitive to weathering and alteration and can remain intact in rocks with strong argillization (Ayers and Watson, 1991; Creaser and Gray, 1992). Moreover, both major and trace elements of apatite, such as Cl, F, S, Sr, REE, Ga, V, and Mn, are considerably sensitive to the changes in magmatic composition and oxidation state (Sha and Chappell, 1999; Tepper and Kuehner, 1999; Belousova et al., 2002; Piccoli and Candela, 2002; Cao et al., 2012). Several experiments showed that apatite can crystallize as a liquidus phase in the felsic magma system (e.g., Watson, 1979, 1980; Harrison and Watson, 1984; Wolf and London, 1994). Given the above facts, it is gradually acknowledged that the apatite can effectively record the initial information of magma, even if its host rocks are not fresh. In this study, the following four representative granitoid plutons in the eastern Tibet are selected: the Pulang pluton, which is associated with porphyry-type Cu deposit and three coeval non Cu-mineralized plutons,

* Corresponding author.
E-mail address: panlichuan@mail.gyig.ac.cn (L.-C. Pan).

https://doi.org/10.1016/j.oregeorev.2020.103757
Received 12 March 2020; Received in revised form 11 August 2020; Accepted 2 September 2020
Available online 13 September 2020
0169-1368/

namely, Cuojiaoma, Dongcuo, and Daocheng. We analyzed the major, minor and trace elements and Nd isotope of apatite from these four plutons using EPMA, LA-ICP-MS and LA-MC-ICP-MS. According to the chemical compositions of apatite and Ce^{4+}/Ce^{3+} ratio of zircon, we identified differences in fertility of causative magmas. Our study provides important insights into the causes of differences in Cu-mineralized potential of Paleo-Tethyan granitoids in eastern Tibet.

2. Geology setting

The Paleo-Tethys Ocean was formed by Devonian-to-Permian seafloor spreading between Gondwana and Laurasia. In East Asia, the Paleo-Tethys Ocean comprises several branches that can be traced by the corresponding suture zones. The Garzê-Litang suture zone, as a remnant of the Garzê-Litang Ocean, is 5–20 km wide and > 500 km long, defining the boundary between the Songpan-Garzê terrane and the Yidun Arc belt. This branch ocean opened in the Late Permian because of either a plume beneath the western margin of the Yangtze Craton (Song et al., 2004; Xiao et al., 2008) or a back arc basin due to the eastward subduction of the Jinshajiang Ocean along the Jinshajiang suture (Roger et al., 2008, 2010), thereby separating the Zhongdian massif from the Yangtze plate. The Garzê-Litang Ocean began to subduct westward beneath the Zhongdian massif in the Late Triassic, forming the Yidun Arc belt in the east of this massif (Mo et al., 1994; Hou et al., 2004). At the end of the Triassic, the Yidun Arc belt eventually collided with the Songpan-Garzê Terrane (Hou et al., 2004; Wang et al., 2011). During the aforementioned subduction and collisional process, abundant granitoids with the ages of 225–202 Ma were developed along the Yidun Arc belt (Hou et al., 2001; Lai et al., 2007; Reid et al., 2007; Weislogel, 2008) (see Fig. 1). Most of them are Cu-barren, and only a few that are located in the southern part of the Yidun Arc belt can form porphyry Cu deposits.

The Pulang pluton, which is located approximately 36 km northeast of Shangri-La city, generates a large porphyry Cu deposit that contains approximately 4.31 Mt Cu (0.34%) and 113 t Au (0.09 g/t) (Li et al., 2011). This pluton mainly comprises quartz diorite porphyry, quartz monzonite porphyry, and granodiorite porphyry (Li et al., 2011) (see Fig. 2a). The majority of Cu orebodies are hosted in the quartz monzonite porphyry that intrudes the quartz diorite porphyry and is cut by granodiorite porphyry (Yang et al., 2019). Some recent zircon U–Pb ages showed that the Pulang pluton was formed in ca. 216 ± 2 Ma (Cao et al., 2018, 2019) or 217–212 Ma (Leng et al., 2018a), which are consistent with the molybdenite Re-Os ages (ca.213–216 Ma), thereby indicating the simultaneous formation of the pluton and deposit (Zeng et al., 2004; Li et al., 2011; Cao et al., 2018, 2019). The whole-rock chemical composition shows an increase in SiO_2 and $K_2O + Na_2O$ contents and K_2O/Na_2O ratio from quartz diorite porphyry to quartz monzonite porphyry and then granodiorite porphyry (Pang et al., 2009). This whole-rock chemical variation, together with isotopic results including zircon εHf(t) (−4.6 to −2.5), and whole-rock $(^{87}Sr/^{86}Sr)_i$ (0.7052 to 0.7102) (Wang et al., 2018) indicate the Pulang pluton formed by multiphase intrusion of a mixture of mantle-and crust-derived magmas (Pang et al., 2009, 2014; Wang et al., 2018). The Cu oredodies are mainly located within the phyllic and potassium silicate alteration zones, occupying the quartz monzonite porphyry (Li et al., 2011). The spatial distribution of orebodies further supports the genetic link between quartz monzonite porphyry and Cu mineralization (Li et al., 2011; Liu et al., 2016; Cao et al., 2018, 2019). The quartz

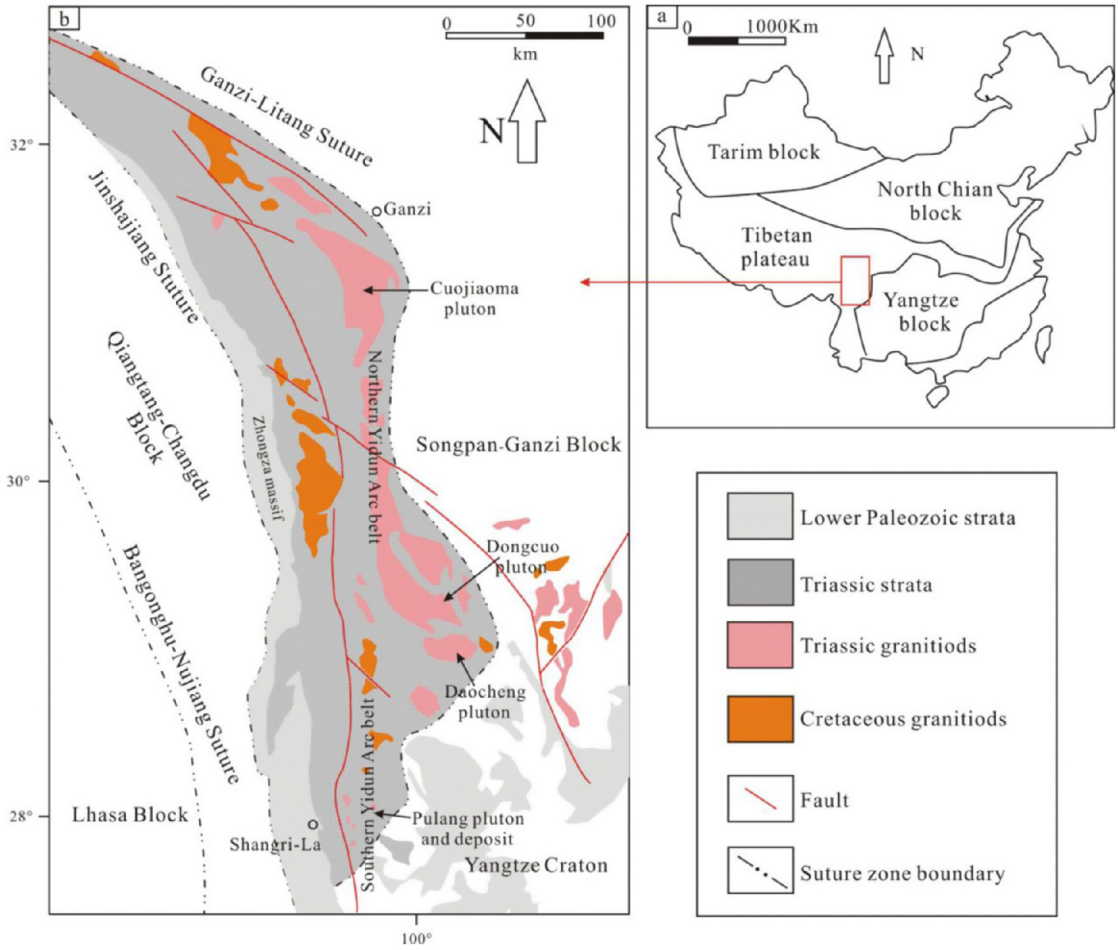

Fig. 1. Regional geological map of the research area (modified from Wang et al., 2014).

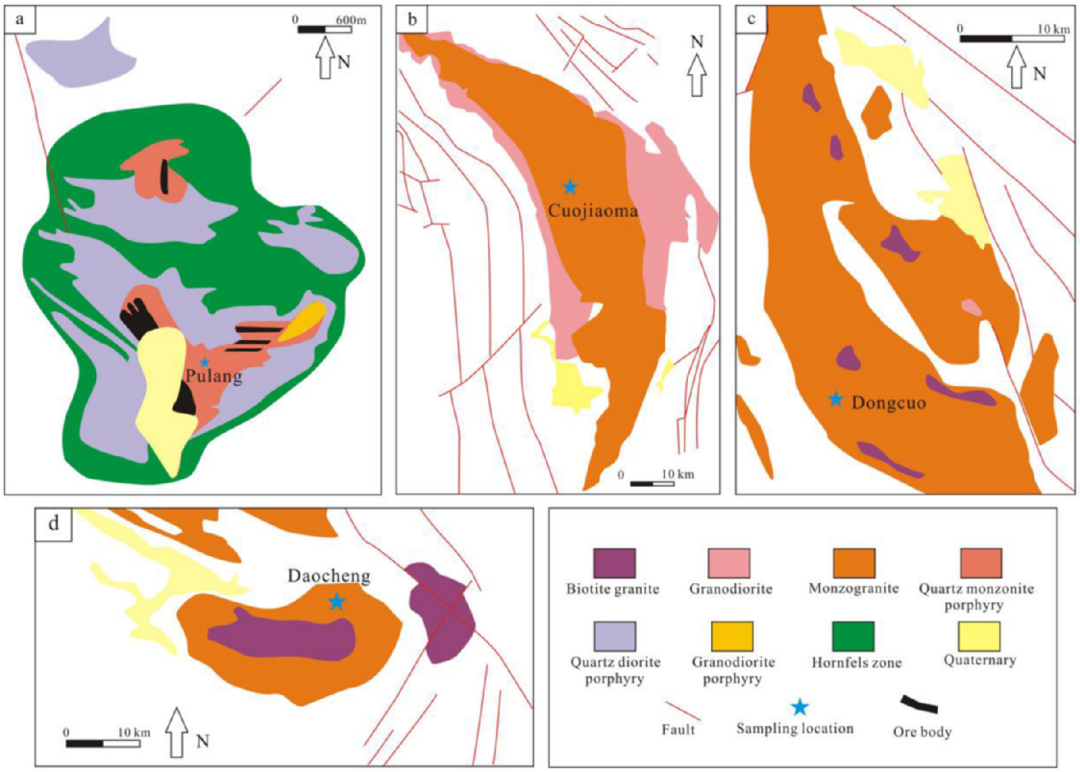

Fig. 2. Simplified geological maps for the Pulang (a), Cuojiaoma (b), Dongcuo (c), and Daocheng (d) plutons.

monzonite porphyry is composed of plagioclase, K-feldspar, biotite and quartz as phenocrysts and a matrix containing fine-grained plagioclase, K-feldspar, biotite and quartz. The accessory minerals include apatite, titanite and zircon. Previous studies showed that the formation of this pluton may be associated with the westward subduction of the Garzê-Litang Ocean (Hou et al., 2003; Wang et al., 2011; Yang et al., 2017). In addition, the long time span (> 50 m.y.) of extremely slow cooling and erosion at Pulang is an important reason for the preservation of this Cu deposit (Leng et al., 2018b).

Notably, Cu-barren plutons are widespread in the northern Yidun Arc belt, and the typical plutons are Cuojiaoma, Dongcuo, and Daocheng. The Cuojiaoma pluton is located approximately 50 km south of the Ganzi city. It is one of the largest granite in the Yidun island Arc belt, covering an area of ~ 4000 km^2. This pluton consists of monzogranite and a small amount of granodiorite (see Fig. 2b). The monzogranite contains quartz (30%), plagioclase (~25%), K-feldspar (25%), biotite (10%) and amphibole (~5%) as major phases and apatite and zircon as accessory phases. The zircon U-Pb age of this pluton is 219 ± 1 Ma (Wu et al., 2017) or 236 ± 1.9 Ma (Wang et al., 2017). The Dongcuo pluton is located approximately 200 km south of the Cuojiaoma pluton, covering an area of > 800 km^2. This pluton is dominated by monzogranite, while biotite granite and granodiorite are sparse (see Fig. 2c). The monzogranite is mainly composed of quartz (25%), K-feldspar (30%), plagioclase (35%), biotite (8%) and amphibole (~2%). The accessory minerals include apatite and zircon. The zircon U-Pb age of this pluton is 222 ± 3 Ma (Wu et al., 2017). The Daocheng pluton is located in the east of the Daocheng city, covering an area of ~ 200 km^2. This pluton is mainly composed of monzogranite and granodiorite (see Fig. 2d). K-feldspar (~35%), plagioclase (~30%), quartz (~20%), and biotite (~10%) are the major phases, and apatite, zircon and allanite are the accessory phases in the monzogranite. The zircon U-Pb ages of this pluton is 220 ± 2 Ma (Wu et al., 2017). In general, the almost similar ages of the aforementioned three plutons imply that they were probably generated in the same geodynamic setting. Nevertheless, the petrogenesis of these granites is still not very clear. Some studies (e.g., Hou et al., 2001; He et al., 2013) proposed that they are derived from partial melting of the Late Paleoproterozoic basement, while others suggested they were derived from metasediments (e.g., Liu et al., 2006). Moreover, the tectonic background in which these granites were formed is interpreted as an arc setting (Wang et al., 2013) or a post-orogenic extensional setting (Peng et al., 2014).

Apatite, as a common accessory phase, occurs widely in the above-mentioned four plutons. This mineral, as euhedral crystals, can be wrapped in K-feldspar and biotite (see Fig. 3). We calculated the apatite-saturation temperatures using the method proposed by Harrison and Watson (1984). The results showed that the four plutons had high apatite-saturation temperatures (> 860°C). This result, together with textural relationship, implies that apatite can crystallize early as a liquidus mineral in the parental magmas of the four plutons. The Cathodoluminescence images show homogeneous luminescence of apatite (Fig. 4), which is different from that of the altered apatite (e.g., Bouzari et al., 2016). Apatite halogens are sensitive to hydrothermal alteration (Palma et al., 2019). Since Cl shows a strong preference for aqueous solutions relative to F (Candela, 1986; Boudreau and Kruger, 1990), hydrothermal fluid alteration can cause the transformation of fluorapatite toward the chlorapatite end member (Palma et al., 2019). As a result, the fluid-modified apatite can have generally high Cl content, typically > 3.0 wt% (Palma et al., 2019). However, the analyzed apatite crystals in this study have generally low Cl content (< 0.55 wt%, see Appendix 1). These above observed morphogenic and compositional features of apatite all suggest that the effect of hydrothermal alteration on the chemistry of apatite is very limited. Therefore, the chemical composition of the apatite crystals investigated might effectively reflect the initial information of magmas.

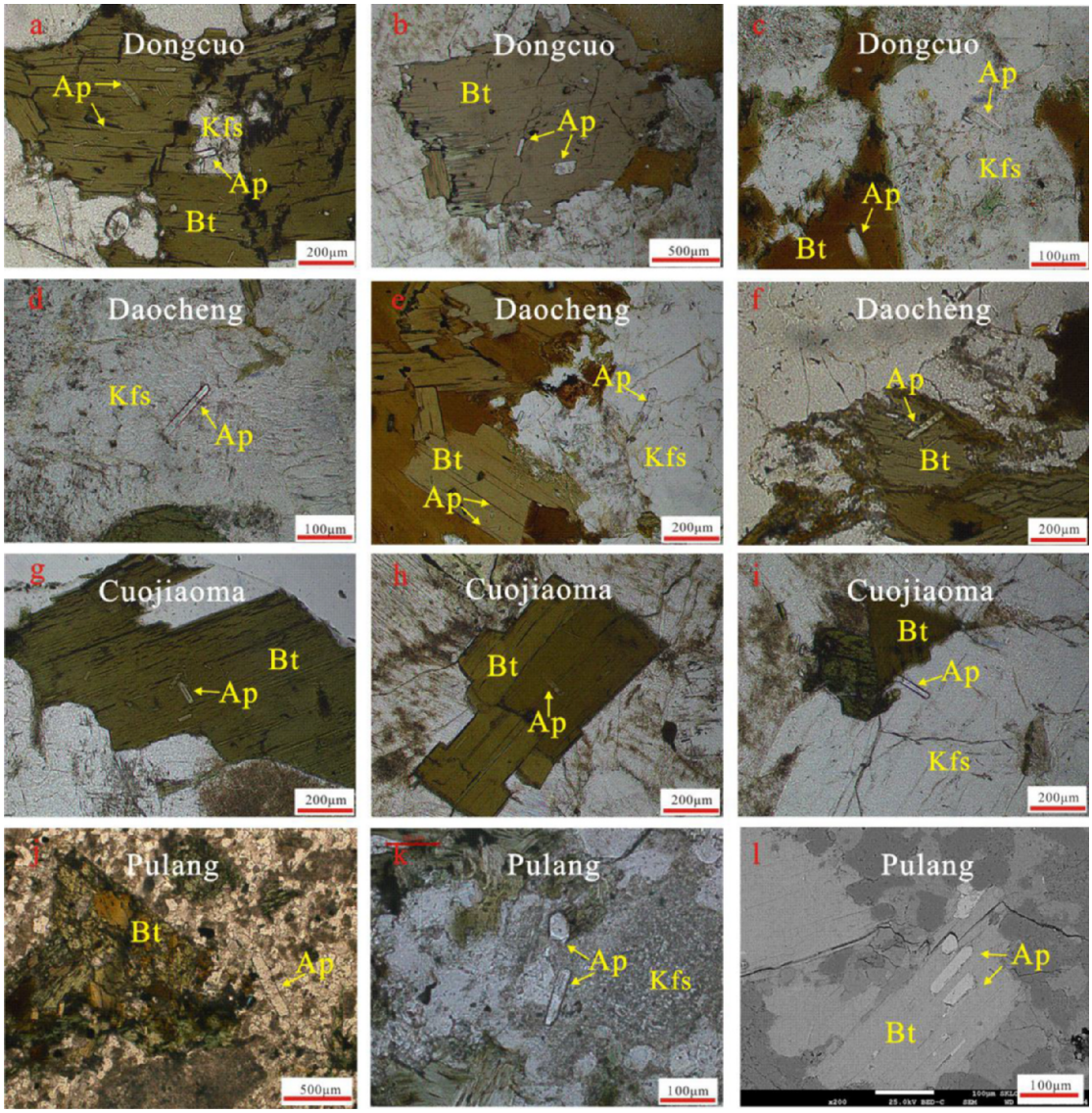

Fig. 3. Modes of the occurrence of apatite in the rock samples from the selected plutons. Ap: apatite; Bt: biotite; Kfs: K-feldspar.

3. Sampling and analytical methods

3.1. Sampling methods

We selected monzogranite that is most widespread in the Cuojiaoma, Dongcuo and Daocheng plutons as the representative of non-mineralized rock and the quartz monzonite porphyry in the Pulang pluton as the representative of Cu-mineralized rock. Eight relatively fresh rock samples were chosen for whole-rock major and trace elemental analysis. Four of them were prepared for apatite and zircon selection. The analyzed zircon and apatite crystals in individual pluton are selected from the same rock sample. Details of the samples are shown in Table 1.

3.2. Whole-rock compositions

The selected rock samples are relatively fresh and do not show significant alteration and weathering. The concentrations of whole-rock major elements were determined using fused lithium-tetraborate glass pellets by employing an Axios PW4400 X-ray fluorescence spectrometer at the State Key Laboratory of Ore Deposit Geochemistry, Institute of Geochemistry, Chinese Academy of Sciences in Guiyang (SKLODG). The analytical precision was estimated to be less than 5%. The concentrations of the trace elements in the whole rocks were analyzed using a PE DRC-e ICP-MS at SKLODG. Powdered samples (50 mg) were dissolved using the mixture of HF and HNO_3 in high-pressure polytetrafluoroethylene vessels for 2 days at approximately 190 °C. Rh was used to monitor the signal drift during the analysis. The detailed analytical procedures are present in Qi et al. (2000). The analytical precision is estimated to be within 10%.

3.3. Major elements compositions of apatite

Apatite crystals were separated from the rocks by using standard heavy-liquid and magnetic methods. Subsequently, the crystals were mounted and polished using epoxy. We used CL images to choose the appropriate targets for the in-situ analysis. The contents of the major and minor elements in apatite were determined using a JEOL-1600 electron microprobe at SKLODG. The analytical conditions were as follows: accelerating voltage of 25 kV, beam current of 10nA, and beam diameter of 10 μm. The following natural minerals were used for calibration: apatite (P, S, F), kaersutite (Ca, Mn, Na, Al, Si, Fe), and tugtupite (Cl).

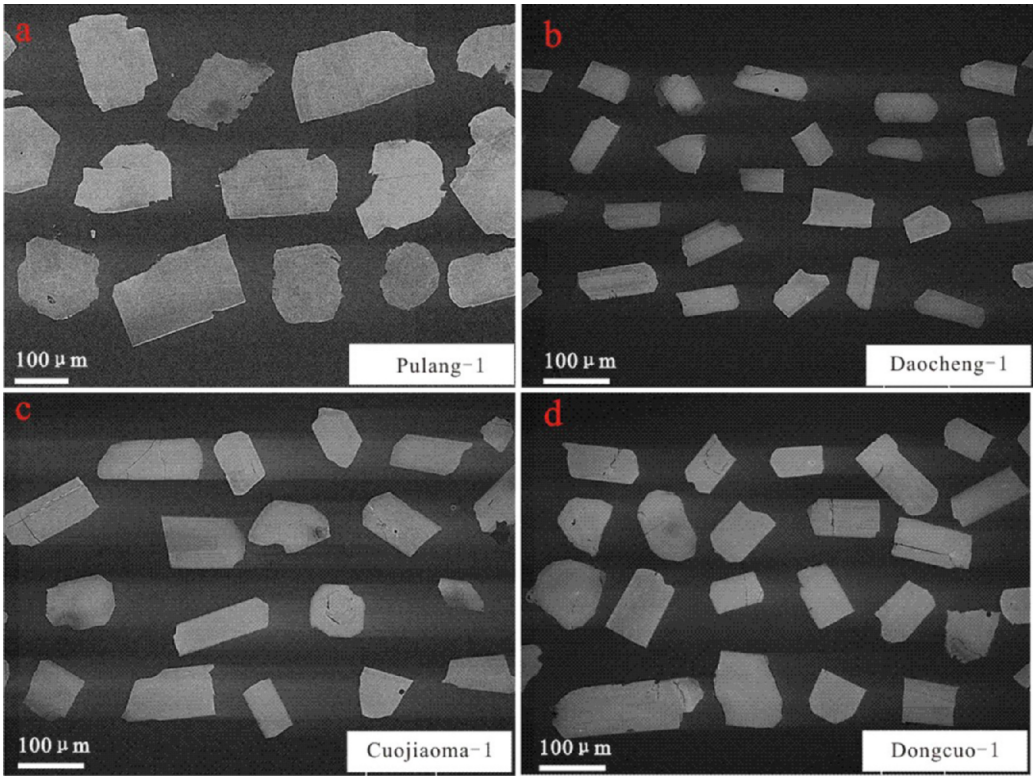

Fig. 4. CL images of the representative apatite crystals from the four plutons for in-situ analysis.

3.4. Trace elements compositions of apatite and zircon

The concentrations of the trace elements in apatite and zircon were measured using in-situ LA-ICP-MS at SKLODG. The LA-ICP-MS system was an Agilent 7500a ICP-MS equipped with a Resonetics RESOLution M-50 ArF-Excimer laser gun (λ = 193 nm, 80 mJ, 10 Hz). The laser-ablation spot was 44 μm in diameter. The ablated aerosol was fed to the ICP instrument using He gas. The NIST610 and NIST612 standards were used for calibration. The content of apatite Ca was normalized for using the concentration determined via electron probe analysis. Off-line data reduction was then performed using the ICPMSDataCal software from Liu et al. (2008).

3.5. Apatite Nd isotope

The in-situ apatite Nd isotope measurements were conducted on an Nu Plasma III MC-ICP-MS (Nu Instruments), which was attached to a RESOlution-155 ArF193-nm laser ablation system (Australian Scientific Instruments) at SKLODG. Apatite was ablated in an atmosphere containing the mixture of helium (350 ml/min) and nitrogen (2 ml/min) using the following parameters: baseline time of 30 s, ablation time of 40 s, spot size of 60–104 μm, repetition rate of 6 Hz, and energy density of 6 J/cm^2. The interference of ^{144}Sm on ^{144}Nd was derived from the ^{147}Sm intensity with the natural ^{144}Sm/^{147}Sm ratio of 0.205484 (Isnard et al., 2005). The mass-bias factor of Sm was calculated using the measured isotopic ratio of ^{147}Sm/^{149}Sm and its true value, i.e., 1.08680 (Isnard et al., 2005). The mass bias of ^{143}Nd/^{144}Nd was normalized to ^{146}Nd/^{144}Nd = 0.7129 using an exponential law. To perform quality control, we implemented one apatite standard, namely, Durango every 5 samples and other two apatite standards, namely, AP1 and MAD, every 30 unknown samples. The measured ^{143}Nd/^{144}Nd ratio for the apatite standard AP1 was 0.512342 ± 0.000014 (n = 12), which was identical to the recommended value (AP1: 0.512352 ± 0.000024) (Yang et al., 2014).

4. Results

4.1. Whole-rock compositions

The major, minor, and trace elemental compositions of the rock samples from the four selected plutons are listed in Table 2. The data therein show that the four plutons are metaluminous and calc-alkaline (see Fig. 5a; b) with the Rittmann index of 1.55–2.81 and A/CNK of 0.94–1.02 The chondrite-normalized trace-element patterns of the samples are depicted in Fig. 5c. All the rock samples are characterized by mild to strong depletion of K, Nb, P, and Ti. From the chondrite-

Table 1
Sample information of the Pulang, Cuojiaoma, Dongcuo and Daocheng plutons.

Pluton	Sample ID	Rock type	Sampling location	Whole-rock analysis	Apatite and zircon selection
Pulang	Pulang-1	Quartz monzonite porphyry	E 99° 59′ 26″	√	√
	Pulang-2		N 28° 02′ 43″	√	
Cuojiaoma	Cuojiaoma-1	Monzogranite	E 99° 46′ 38″	√	√
	Cuojiaoma-2		N 31° 09′ 31″	√	
Dongcuo	Dongcuo-1	Monzogranite	E 100° 04′ 43″	√	√
	Dongcuo-2		N 29° 18′ 46″	√	
Daocheng	Daocheng-1	Monzogranite	E 100° 24′ 17″	√	√
	Daocheng-2		N 29° 02′ 17″	√	

Table 2
The results of major (wt.%) and trace elements (ppm) analyzes for the Cuojiaoma, Dongcuo, Daocheng and Pulang plutons.

Pluton	Cuojiaoma		Dongcuo		Daocheng		Pulang	
SiO2	71.72	70.73	71.15	69.99	72.21	72.64	65.15	62.08
Al2O3	14.01	14.52	14.26	14.64	13.9	13.93	14.32	14.92
TFe2O3	3.01	3.50	3.24	3.62	2.95	2.90	4.27	3.86
MgO	0.69	0.79	1.02	0.96	0.66	0.65	2.51	3.92
CaO	2.76	2.92	2.78	3.09	2.47	2.38	2.68	3.51
Na2O	3.21	3.33	3.23	3.32	3.3	3.3	3.28	4.02
K2O	3.23	3.46	3.62	3.16	3.56	3.54	4.25	2.68
P2O5	0.06	0.07	0.07	0.07	0.06	0.06	0.38	0.34
TiO2	0.28	0.32	0.37	0.39	0.3	0.31	0.5	0.68
MnO	0.06	0.07	0.06	0.07	0.06	0.06	0.02	0.02
L.O.I.	0.47	0.55	0.28	0.61	0.42	0.31	1.85	2.98
Total	99.5	100.26	100.08	99.92	99.89	100.08	99.21	99.01
Na2O + K2O	6.44	6.79	6.85	6.48	6.86	6.84	7.53	6.70
A/CNK	1.01	1.00	1.00	1.01	1.01	1.02	0.96	0.94
Fe^{3+}/Fe^{2+}	0.19	0.21	0.13	0.14	0.10	0.15	0.43	0.38
Rittmann index	1.55	1.79	1.79	1.68	1.73	1.69	2.81	2.63
AST(°C)	872	877	881	869	877	881	1008	958
Ga	16.84	17.58	17.26	16.63	16.00	16.11	17.05	20.42
Rb	126	136	152	119	132	134	155	143
Ba	991	1051	702	772	705	748	1232	885
Sr	235	240	167	191	153	160	665	718
Zr	163	161	206	157	163	139	157	149
Nb	8.94	9.58	12.37	10.58	10.08	10.58	13.73	9.58
Hf	4.19	4.17	6.08	4.26	4.49	3.78	4.28	3.98
Ta	0.89	0.88	1.36	0.91	1.11	1.22	1.22	0.64
Th	18.32	20.21	20.95	14.42	17.47	17.05	17.79	14.32
U	2.32	2.42	4.58	3.11	2.98	2.79	3.54	3.57
La	32.78	38.99	38.32	35.17	31.16	29.24	27.52	28.29
Ce	60.18	71.65	65.09	63.36	62.68	59.79	56.13	59.79
Pr	5.95	7.00	7.39	7.03	6.37	5.92	6.11	6.85
Nd	21.48	25.34	24.92	25.55	23.67	22.63	25.34	28.89
Sm	3.90	4.25	5.38	5.13	4.62	4.17	4.38	5.39
Eu	0.83	0.83	0.85	1.00	0.77	0.84	1.29	1.32
Gd	3.49	3.92	4.53	4.71	4.61	4.53	3.59	3.92
Tb	0.57	0.62	0.74	0.74	0.81	0.69	0.58	0.61
Dy	3.54	4.10	4.51	4.54	4.89	4.44	2.78	3.25
Ho	0.74	0.85	0.96	1.00	1.01	0.93	0.55	0.59
Er	2.17	2.52	2.84	2.49	2.96	2.76	1.36	1.60
Tm	0.33	0.39	0.46	0.38	0.46	0.43	0.18	0.22
Yb	2.27	2.63	3.10	2.61	2.92	2.70	1.46	1.47
Lu	0.37	0.38	0.43	0.37	0.46	0.44	0.18	0.20
Y	22.95	26.21	30.21	28.11	29.05	26.63	16.53	16.95
ΣREE	139	163	160	154	147	140	131	142
δEu	0.69	0.62	0.52	0.62	0.51	0.59	0.99	0.88
δCe	1.06	1.06	0.95	0.99	1.09	1.11	1.06	1.05

Rittmann index = $(Na_2O + K_2O)^2/(SiO_2 - 43)$, $\delta Eu = Eu_N/(Sm_N \times Gd_N)^{1/2}$, $\delta Ce = Ce_N/(La_N \times Pr_N)^{1/2}$.
AST: apatite saturation temperatures that are calculated by the formula from Harrison and Watson (1984).

normalized REE diagram, it is evident that all the samples display fractionated REE patterns (see Fig. 5d). Among the four plutons, the Pulang pluton is classified as an adakite-like rock that is characterized by abundant Sr (> 400 ppm), scarce Y (< 20 ppm) and Yb (< 2 ppm), and high values of $(La/Yb)_N$ (> 15) and δEu (> 0.80). The other three plutons are not adakite-like rock. They have much lower Sr/Y, La/Yb, and δEu values than the Pulang pluton.

4.2. Apatite composition

The ideal chemical formula for apatite is $Ca_5(PO_4)_3F$. The Ca position is usually substituted by REE^{3+}, Mn^{2+}, Na^+, Sr^{2+}, and Ga^{2+}. The P^{5+} position is usually substituted by S^{4+}, Si^{4+}, and V^{5+}. The F^- position is mainly substituted by Cl^- and OH^-.

4.2.1. Major and minor elements

The major and minor elemental compositions of the apatite are listed in Appendix 1. In the selected four plutons, the CaO contents of apatite vary from 54.27 to 55.74 wt%. The contents of Na_2O and MnO are less than 0.19 wt%, and the SiO_2 in apatite is almost undetectable via EPMA. The apatite CaO does not show a clear negative correlation with MnO and Na_2O, suggesting the inconsequential substitutions of Ca by Mn and Na. However, the observed negative correlation between apatite CaO and REE (see Fig. 6a) indicates the main substitution of Ca by REE via the reaction including the following: $2REE^{3+} + [V] = 3Ca^{2+}$ (1), $REE^{3+} + Na^+ = 2Ca^{2+}$ (2), and $REE^{3+} + Si^{4+} = Ca^{2+} + P^{5+}$ (3) (RØnsbo, 1989; Sha and Chappell, 1999; Pan and Fleet, 2002). Reactions (2) and (3) may play secondary roles in apatite-Ca substitution because of the extremely low Si and Na contents in apatite. The P_2O_5 content is consistent in the selected apatites (39.41–41.68 wt %). The apatite SO_3 content in the Pulang pluton varies from 0.19 to 0.31 wt%, which is considerably higher than those in the other three plutons (< the detected limit of EPMA). The observed negative correlation between apatite SO_3 and P_2O_5 in the Pulang pluton (see Fig. 6b) can be attributed to the substitution of P by S via the following reaction: $Na^+ + S^{6+} = Ca^{2+} + P^{5+}$ (4) (Sha and Chappell, 1999). All the apatite crystals are F–rich (F: 2.18–3.14 wt%) and Cl-barren (Cl: < 0.54 wt%). The negative correlation between apatite F and Cl in the Pulang pluton (see Fig. 6c) suggests the substitution of F by Cl (Pan and Fleet, 2002). However, in the other three plutons, apatite F does not show any correlation with apatite Cl, which may be because of the dominant substitution of F by OH^- in these apatites.

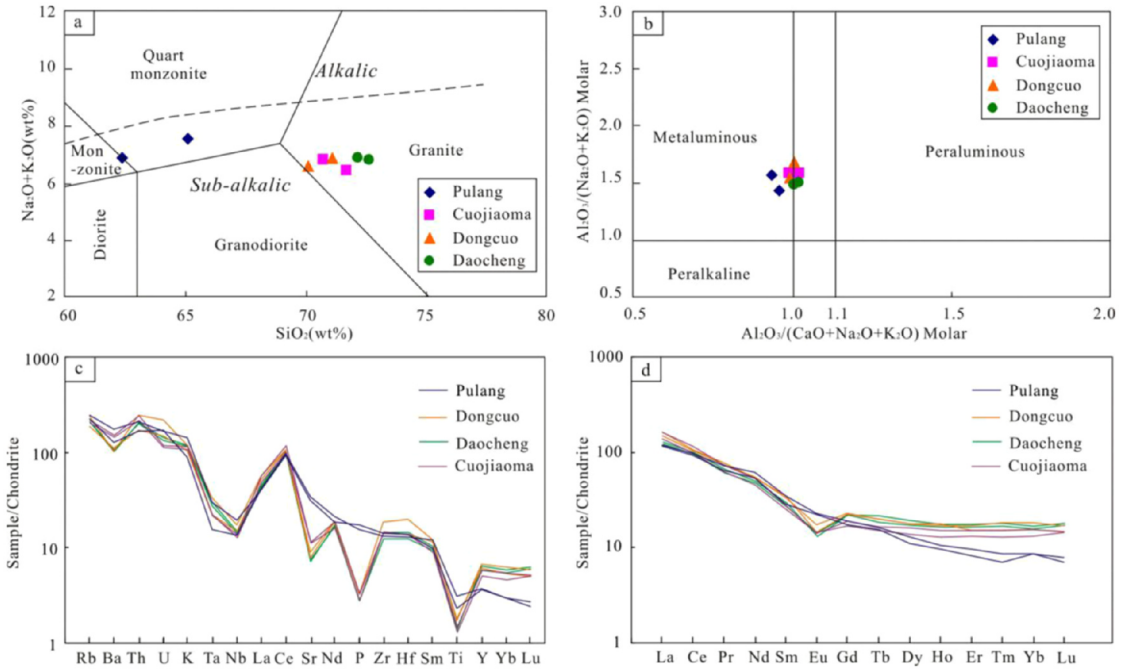

Fig. 5. Total alkali versus SiO_2 diagram (Middlemost 1994) (a), A/NK versus A/CNK diagram (Maniar and Piccoli, 1989) (b), Chondrite-normalized trace-element diagrams (c), and REE diagrams (d) for the Pulang, Cuojiaoma, Dongcuo, and Daocheng plutons. Data are listed in Table 2. The chondrite values are from Sun and McDonough (1989).

4.2.2. Trace elements

The trace-element compositions of the apatite are listed in Appendix 1. The apatite crystals from the four plutons show abundant REE (3636–10247 ppm), Y (179–3178 ppm), Sr (72.49–434 ppm), Th (9.02–101 ppm), and U (4.20–35.54 ppm). The observed positive correlations among apatite Th, U, Ga, Y, and REE (see Fig. 6d–f) imply the similar behavior of these elements as a substitute of apatite Ca. Apatite can incorporate an amount of Cu because of the substitution of Ca by Cu (Wang et al., 2016). Our result shows that the apatite Cu content in the Pulang pluton (0.02–0.55 ppm, with an average of 0.16 ppm) is considerably higher than those in the other three plutons (< 0.13 ppm; with an average of 0.03 ppm). The higher Cu may be due to Cu-bearing inclusion in apatite, similar to Cu-bearing inclusion in zircon (e.g., Lu et al., 2016). But this scenario can be ruled out in Pulang's apatite for the following reasons. First, the apatite Cu content is generally high (> 0.10 ppm), which seems to be contradictory to rare Cu-bearing inclusions in apatite. In addition, if Cu-bearing inclusion is ablated, time-resolved LA-ICP-MS spectra of Cu should show spike, which, however, did not be observed during laser ablation period. Therefore, we believe that Cu is incorporated into apatite structure and Cu content of apatite is controlled by Cu partitioning between apatite and melt. The negative correlation of apatite V and P_2O_5 in the Pulang pluton (see Fig. 6g) indicates the substitution of P by V. The positive correlation of apatite SO_3 and V (see Fig. 6h) demonstrates their similar behavior as a substitute of apatite P. The chondrite-normalized REE patterns of apatite from the four plutons show the enrichment in light REE relative to heavy REE and the significantly negative Eu anomaly (see Fig. 7). The apatite crystals from the Pulang pluton contain considerably higher La/Yb ratio and δEu than those from the other three plutons, thereby agreeing with the REE pattern features in the host rocks for these apatites.

4.3. Apatite Nd isotope

The apatite in-situ Nd isotopic data are listed in Table 3. The data show that apatite εNd(0) values are −6.5 to −3.3, −9.6 to −6.4, −10.4 to −5.3 and −9.9 to −5.2 in the Pulang, Dongcuo, Cuojiaoma and Daocheng plutons, respectively. We calculated the apatite εNd(t) values based on the reported zircon ages of these four plutons (Cao et al., 2018; Wu et al., 2017). The result shows that the Pulang pluton has relatively high apatite εNd(t) values (−3.8 to − 0.9). The Cuojiaoma, Dongcuo, and Daocheng plutons have relatively low apatite εNd(t) values, which are − 8.2 to − 3.7, –8.0 to –4.7, and –8.7 to –4.2, respectively.

4.4. Trace elements of zircon

The average contents of zircon trace elements are shown in Table 4. The high Th/U ratios (> 0.1) suggest that the selected zircon crystals are igneous. The average Ce contents of zircon are 29.95, 6.05, 5.07, and 5.22 ppm in the Pulang, Cuojiaoma, Dongcuo, and Daocheng plutons, respectively. We calculated the zircon Ce^{4+}/Ce^{3+} ratio using the method proposed by Ballard et al. (2002) to evaluate the magmatic oxygen fugacity. The result reveals that the Pulang pluton has considerably higher zircon Ce^{4+}/Ce^{3+} ratio (the average of 279) than those of the Cuojiaoma, Dongcuo, and Daocheng plutons (the average of 18, 25, and 32 respectively).

5. Discussions

5.1. Comparison of magmatic oxidation states between granitoids

The high magmatic oxygen fugacity might promote the porphyry Cu mineralization because in oxidized conditions, Cu can be more easily transported by magma to upper crustal levels and, consequently, become highly concentrated in ore-forming magmatic fluids (Ballard et al., 2002; Richards, 2015a). The whole-rock Fe^{3+}/Fe^{2+} ratio is a common indicator to evaluate the magmatic oxidation state. Our results show that the Pulang pluton has considerably higher whole-rock Fe^{3+}/Fe^{2+} ratios (0.38–0.43) than those of the other three plutons (0.10–0.21), thereby implying that the former pluton was formed by a relatively oxidized magma system. However, this conclusion attained using the whole-rock compositions must be verified using other methods because of the weathering and alteration of the rock samples.

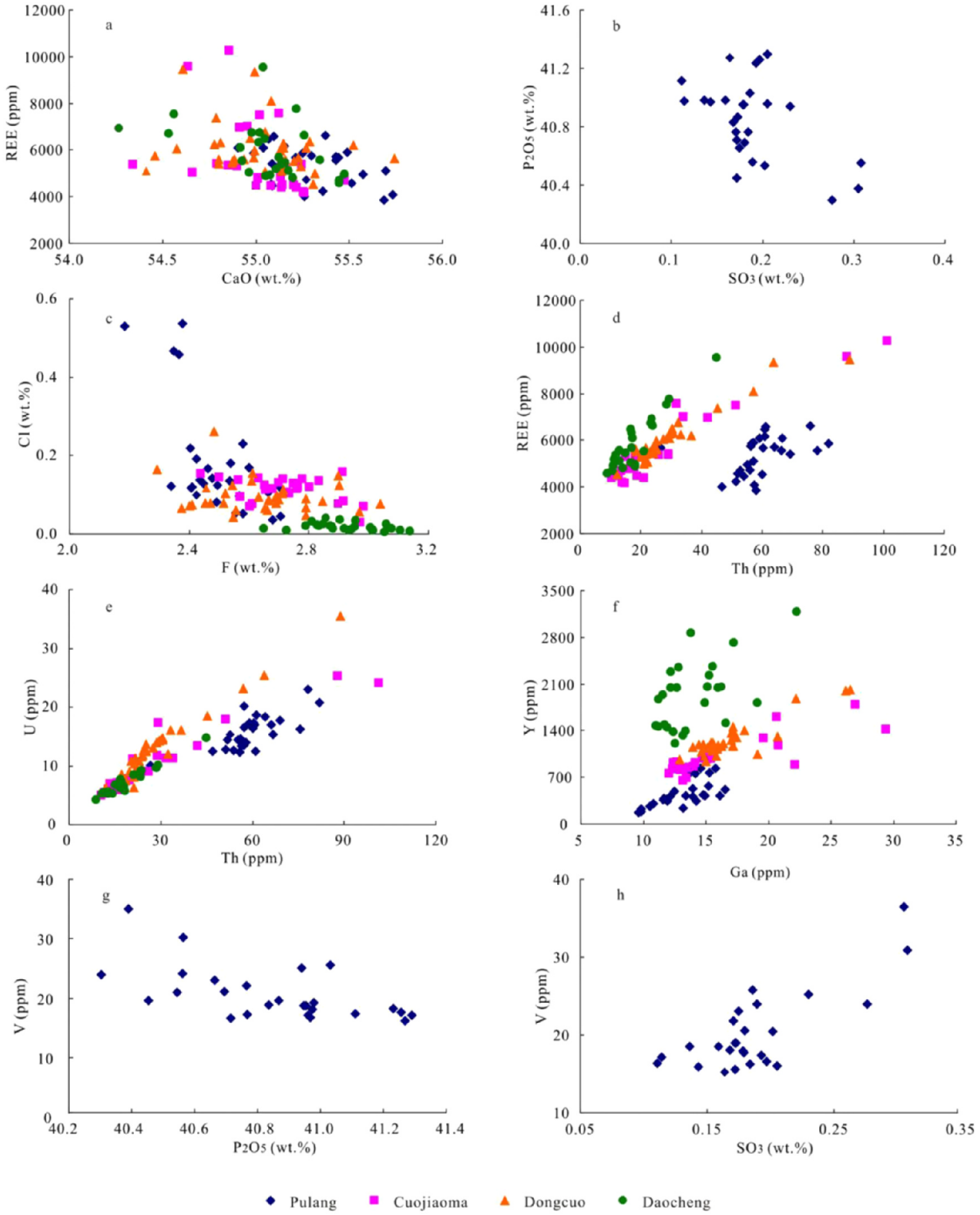

Fig. 6. Plots of CaO versus REE (a), SO_3 versus P_2O_5 (b), F versus Cl (c), Th versus REE (d), Th versus U (e), Ga versus Y (f), and SO_3 versus V (g) in the apatites from the selected plutons.

Numerous studies showed that apatite trace elements such as Mn, Eu, Ce, and Ga can be used to identify the magmatic oxidation state (e.g., Sha and Chappell, 1999; Imai, 2002, 2004; Cao et al., 2012; Sun et al., 2019). Mn^{2+}, Eu^{3+}, Ce^{3+}, and Ga^{2+} have similar cation radii and valences to those of Ca^{2+} (Piccoli and Candela, 2002) and, therefore, can be incorporated into apatite to easily substitute Ca^{2+}. Consequently, the apatites that crystallize from the oxidized magma that primarily comprises high-valence cations would contain more Eu but less Ce, Ga, and Mn, compared with apatites that crystallize from less oxidized magma, provided that the elemental contents are similar in both the magma systems. Unfortunately, the elemental contents are not usually consistent in different magma systems. For example, the Pulang pluton shows the lowest whole-rock MnO content among the four plutons. Therefore, it is unclear whether the lowest apatite MnO in the Pulang pluton is attributed to either the high magmatic oxidation state or low Mn content in magma. In addition, the positive correlation between apatite δEu and Sr indicates a significant control of magmatic δEu via feldspar crystallization (Bi et al., 2002).

Despite the limitations, magmatic oxidization state can be validly evaluated by comparing the change in the above-mentioned indexes in apatites and their host rock. We observed that the apatite from the Pulang pluton contained lower Ga content and δCe value compared with that from the other three plutons, but the lower whole-rock Ga content and δCe value could not be displayed in the Pulang pluton (see

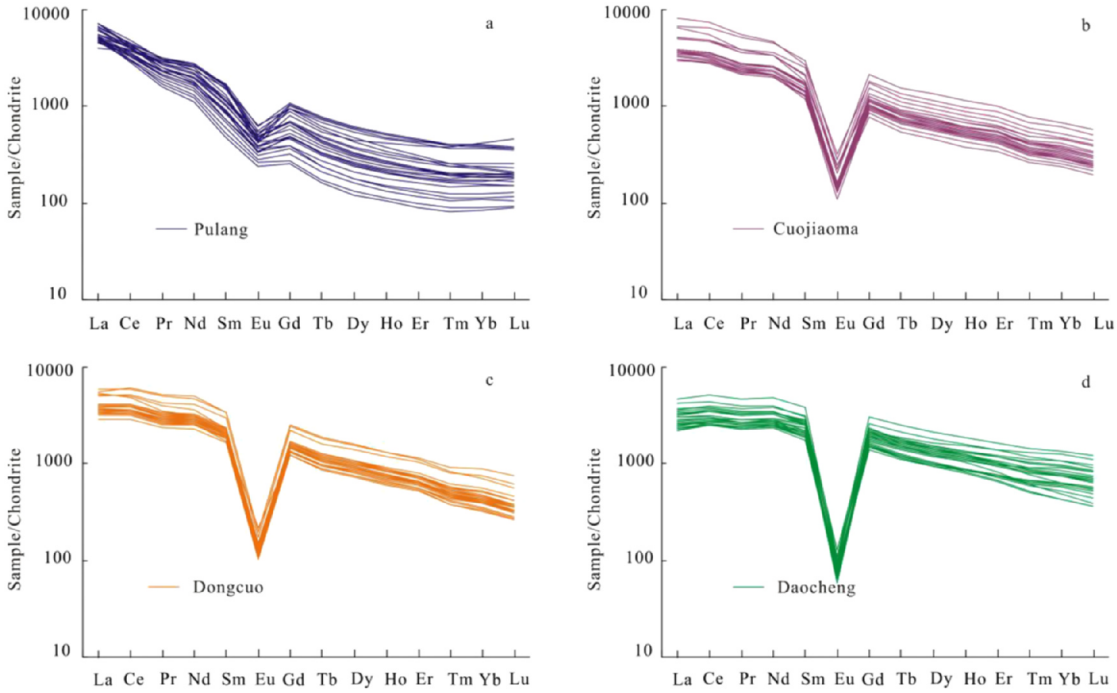

Fig. 7. Chondrite-normalized REE patterns for the apatite crystals from the selected plutons. Data are listed in Appendix 1. The chondrite values are from Sun and McDonough (1989).

Fig. 8a; b). This compositional decoupling between apatite and whole rock infers that the Ga and Ce variations in apatite mainly depend on the magmatic oxidization state rather than the magmatic composition. The higher magmatic oxygen fugacity, therefore, can be expected in the Pulang pluton to prevent more Ce and Ga from incorporating into these apatite crystals, and lead to poor Ga and Ce in apatites, although the magma for this apatite is not deficient in these two elements. To test this finding, we estimate the magmatic oxygen fugacity on the basis of zircon Ce^{4+}/Ce^{3+} ratios calculated using the method proposed by Ballard et al. (2002). The result shows that the Pulang pluton has considerably higher zircon Ce^{4+}/Ce^{3+} ratio (279) than those of the other three plutons (zircon Ce^{4+}/Ce^{3+} ratio: 18–32). This result is consistent with the variation in apatite Ga and whole-rock Fe^{3+}/Fe^{2+} ratio (see Fig. 8c), thereby confirming a more oxidized magma system in the Cu-mineralized Pulang pluton.

5.2. Comparison of magmatic metal and volatile abundances in granitoids

In porphyry metallogenic systems, the ore-forming elements mainly come from magma. Therefore, the concentrations of Cu, S, and Cl in magma are the crucial proxies to evaluate the Cu-mineralization potential of porphyry (Cline and Bodnar, 1991; Richards, 2015a). However, using whole-rock samples, one may fail to estimate these elemental abundances in magma because the rock associated with Cu mineralization is always mixed with hydrothermal Cu-bearing sulfides, thereby overestimating the Cu in magma. Furthermore, magmatic Cl and S cannot be entirely preserved in rocks because of their exhaustion during hydrothermal exsolution and degassing. Therefore, the contents of Cu, S, and Cl in the apatite that can early crystallize from magma rather than those in the rock sample are the better indicators for the abundance of magmatic metals and volatiles. Compared with Cl and S, less attention is paid to Cu of apatite in the past. A recent study (Wang et al., 2016) showed that Cu-bearing apatite (Cu content may exceed 1 wt%) could be synthesized in high Cu solution. However, natural apatite can not have such a high Cu content, which may be attributed to low Cu concentration in the magma. Although there is no study on the partitioning of Cu between apatite and melt, the synthesis of Cu-bearing apatite (Wang et al., 2016) suggests that the content of Cu in apatite may be mainly determined by the concentration of Cu in the coexisting fluid or melt system.

Our data show that the Pulang pluton has nearly an order of magnitude higher apatite SO_3 and Cu content than those of the other three plutons (see Fig. 9a), thereby implying a more S and Cu-rich magma system in the Pulang pluton relative to the other three plutons. The aforementioned statement is reasonable in consideration of the Pulang pluton's higher magmatic oxygen fugacity, which promotes the decomposition of sulfides in the magma source to form the S- and Cu- rich parental magma. However, the low S and Cu contents in apatites from the Cuojiaoma, Daocheng, and Dongcuo plutons are associated with the low magmatic oxygen fugacity, which not only hinders the melting of sulfides from the sources but also facilitates the early saturation of the Cu-bearing sulfide during fractional crystallization. This latter process may not be important because of the lack of paragenesis between apatite and sulfide. In addition, the apatites from the Pulang pluton showed higher Cl contents than those from the other three plutons (see Fig. 9b; c), suggesting that the Cu-mineralized magma is more Cl-rich as apatite crystallized, although hydrothermal exsolution may result in the loss of Cl in apatite, as indicated by the variation in apatite F/Cl ratios (Boudreau and McCallum, 1989; Boudreau and Kruger, 1990; Meurer and Boudreau, 1996; Schisa et al., 2015). The exsolution of the Cl-bearing fluids would extract Cu from the melt in the form of the Cl-complex (Candela and Holland, 1984; Williams-Jones et al., 1995; Webster, 2004). The apatite crystallized from this melt would show simultaneous decrease in Cu and Cl. But the lack of positive correlation between apatite Cu and Cl contents suggests that the exsolution of Cl-bearing fluids has a negligible effect on the magmatic Cu variation, probably because of its small scale in early magma stage. Generally, the content variations of Cu, S, and Cl in apatite indicate that the parental magma of the Cu-mineralized Pulang pluton is more metal- and volatile-fertile than those of the three non-mineralized plutons.

5.3. Reasons for the differences in magmatic fertility between granitoids

The above-mentioned considerable magmatic differences between

Table 3
Nd isotopic compositions of apatites from the Pulang, Cuojiaoma, Dongcuo and Daocheng plutons.

Pluton	$^{143}Nd/^{144}Nd$	2SD	$^{147}Sm/^{144}Nd$	2SD	Age (Ma)	εNd (0)	εNd (t)	2SD
Pulang	0.512349	0.000052	0.097596	0.000126	216 ± 2	−5.6	−2.8	1.0
	0.512324	0.000044	0.117312	0.000280	216 ± 2	−6.1	−3.8	0.9
	0.512383	0.000092	0.097322	0.000140	216 ± 2	−5.0	−2.2	1.8
	0.512385	0.000084	0.118240	0.000340	216 ± 2	−4.9	−2.8	1.7
	0.512469	0.000096	0.109133	0.000640	216 ± 2	−3.3	−0.9	1.9
	0.512396	0.000042	0.140502	0.000560	216 ± 2	−4.7	−3.0	0.9
	0.512383	0.000062	0.114642	0.000320	216 ± 2	−5.0	−2.6	1.2
	0.512373	0.000058	0.132709	0.000100	216 ± 2	−5.2	−3.3	1.2
	0.512341	0.000066	0.112023	0.000340	216 ± 2	−5.8	−3.3	1.3
	0.512307	0.000116	0.100028	0.000220	216 ± 2	−6.5	−3.8	2.3
	0.512376	0.000070	0.097425	0.000076	216 ± 2	−5.1	−2.3	1.4
	0.512366	0.000038	0.116858	0.000064	216 ± 2	−5.3	−3.0	0.8
	0.512358	0.000056	0.101708	0.000054	216 ± 2	−5.5	−2.7	1.1
	0.512320	0.000050	0.108053	0.000174	216 ± 2	−6.2	−3.6	1.0
	0.512400	0.000054	0.110670	0.000114	216 ± 2	−4.6	−2.1	1.1
	0.512412	0.000036	0.120669	0.000150	216 ± 2	−4.4	−2.2	0.7
	0.512341	0.000044	0.105182	0.000078	216 ± 2	−5.8	−3.1	0.9
	0.512438	0.000148	0.113613	0.000320	216 ± 2	−3.9	−1.6	2.9
	0.512359	0.000052	0.138226	0.000720	216 ± 2	−5.5	−3.7	1.0
Dongcuo	0.512289	0.000062	0.148411	0.000156	222 ± 3	−6.8	−5.4	1.2
	0.512231	0.000082	0.153778	0.000280	222 ± 3	−7.9	−6.7	1.6
	0.512168	0.000072	0.148388	0.000158	222 ± 3	−9.2	−7.8	1.4
	0.512231	0.000094	0.139423	0.000280	222 ± 3	−7.9	−6.3	1.2
	0.512299	0.000072	0.148760	0.000420	222 ± 3	−6.6	−5.2	1.8
	0.512288	0.000088	0.159529	0.000300	222 ± 3	−6.8	−5.8	1.4
	0.512312	0.000064	0.141881	0.000240	222 ± 3	−6.4	−4.7	1.3
	0.512150	0.000078	0.139437	0.000260	222 ± 3	−9.5	−7.8	1.5
Dongcuo	0.512230	0.000052	0.153753	0.000380	222 ± 3	−8.0	−6.6	1.0
	0.512218	0.000054	0.145689	0.000172	222 ± 3	−8.2	−6.6	1.1
	0.512157	0.000068	0.147613	0.000100	222 ± 3	−9.4	−7.9	1.3
	0.512145	0.000054	0.143445	0.000162	222 ± 3	−9.6	−8.0	1.1
	0.512270	0.000056	0.150537	0.000122	222 ± 3	−7.2	−5.7	1.1
	0.512210	0.000054	0.154177	0.000320	222 ± 3	−8.3	−7.0	1.1
	0.512253	0.000052	0.149007	0.000136	222 ± 3	−7.5	−6.0	1.0
	0.512170	0.000066	0.144128	0.000130	222 ± 3	−9.1	−7.5	1.3
	0.512152	0.000064	0.145961	0.000128	222 ± 3	−9.5	−7.9	1.3
	0.512187	0.000062	0.149886	0.000106	222 ± 3	−8.8	−7.4	1.2
	0.512227	0.000062	0.148942	0.000280	222 ± 3	−8.0	−6.7	1.7
	0.512254	0.000058	0.157180	0.000300	222 ± 3	−7.5	−6.4	1.1
Cuojiaoma	0.512198	0.000048	0.133063	0.000136	219 ± 1	−8.6	−6.7	1.0
	0.512176	0.000056	0.141314	0.000168	219 ± 1	−9.0	−7.3	1.1
	0.512104	0.000072	0.120385	0.000176	219 ± 1	−10.4	−8.2	1.4
	0.512218	0.000106	0.132329	0.000122	219 ± 1	−8.2	−6.4	2.1
	0.512165	0.000056	0.134593	0.000240	219 ± 1	−9.2	−7.4	1.1
	0.512279	0.000120	0.138250	0.000580	219 ± 1	−7.0	−5.4	2.3
	0.512221	0.000064	0.141469	0.000220	219 ± 1	−8.1	−6.5	1.3
	0.512156	0.000060	0.138468	0.000220	219 ± 1	−9.4	−7.7	1.2
Cuojiaoma	0.512176	0.000052	0.136724	0.000104	219 ± 1	−9.0	−7.2	1.0
	0.512190	0.000044	0.144164	0.000146	219 ± 1	−8.7	−7.1	0.9
	0.512203	0.000056	0.145056	0.000280	219 ± 1	−8.5	−6.9	1.1
	0.512165	0.000068	0.119767	0.000112	219 ± 1	−9.2	−7.0	1.3
	0.512239	0.000070	0.122096	0.000220	219 ± 1	−7.8	−5.6	1.4
	0.512192	0.000040	0.136236	0.000172	219 ± 1	−8.7	−6.9	0.8
	0.512368	0.000134	0.140390	0.000740	219 ± 1	−5.3	−3.7	2.6
	0.512132	0.000104	0.130991	0.000700	219 ± 1	−9.9	−8.0	2.0
	0.512260	0.000100	0.118171	0.000150	219 ± 1	−7.4	−5.2	2.0
	0.512212	0.000072	0.126762	0.000220	219 ± 1	−8.3	−6.4	1.4

(*continued on next page*)

Table 3 (*continued*)

Pluton	$^{143}Nd/^{144}Nd$	2SD	$^{147}Sm/^{144}Nd$	2SD	Age (Ma)	εNd (0)	εNd (t)	2SD
	0.512269	0.000056	0.170785	0.000280	220 ± 2	−7.2	−6.5	1.1
	0.512268	0.000078	0.180026	0.000520	220 ± 2	−7.2	−6.8	1.5
	0.512254	0.000094	0.159189	0.000660	220 ± 2	−7.5	−6.4	1.8
	0.512156	0.000088	0.161320	0.000480	220 ± 2	−9.4	−8.4	1.7
	0.512369	0.000090	0.160661	0.000360	220 ± 2	−5.2	−4.2	1.8
	0.512182	0.000064	0.173328	0.000340	220 ± 2	−8.9	−8.1	1.3
Daocheng	0.512180	0.000076	0.178173	0.001460	220 ± 2	−8.9	−8.3	1.5
	0.512242	0.000088	0.171088	0.000420	220 ± 2	−7.7	−6.9	1.7
	0.512129	0.000084	0.158485	0.000300	220 ± 2	−9.9	−8.7	1.7
	0.512174	0.000060	0.158272	0.000420	220 ± 2	−9.0	−7.8	1.2
	0.512255	0.000080	0.200711	0.001040	220 ± 2	−7.5	−7.5	1.6
	0.512239	0.000072	0.215822	0.000860	220 ± 2	−7.8	−8.2	1.4
	0.512232	0.000080	0.172133	0.000500	220 ± 2	−7.9	−7.1	1.6
Daocheng	0.512135	0.000084	0.160081	0.000640	220 ± 2	−9.8	−8.7	1.7
	0.512220	0.000066	0.181398	0.000480	220 ± 2	−8.1	−7.6	1.3
	0.512137	0.000060	0.152280	0.000360	220 ± 2	−9.8	−8.4	1.2
	0.512220	0.000064	0.164301	0.000560	220 ± 2	−8.1	−7.2	1.2

The ages of these four plutons are cited from Cao et al. (2018) and Wu et al. (2017).

Table 4
The average concentrations (ppm) of trace elements of zircons in the Dongcuo, Daocheng, Cuojiaoma and Pulang plutons.

Pluton	Dongcuo	Daocheng	Cuojiaoma	Pulang
Zircon	n = 9	n = 9	n = 9	n = 7
La	0.07	0.19	0.05	0.09
Ce	5.07	5.22	6.05	29.95
Pr	0.12	0.10	0.13	0.08
Nd	1.49	1.04	2.33	1.33
Sm	3.15	2.17	4.67	3.09
Eu	0.28	0.14	0.72	1.44
Gd	19.94	15.25	26.99	18.70
Tb	7.48	5.95	9.47	6.45
Dy	98.17	79.54	118.19	78.42
Ho	40.69	32.96	47.76	30.60
Er	196	159	224	147
Tm	43.02	33.81	47.60	32.85
Yb	411	314	456	327
Lu	88.23	66.15	94.72	70.25
Hf	12,337	12,413	10,821	11,479
Th	271	167	245	412
U	650	419	443	401
Ce^{4+}/Ce^{3+}	25	32	18	279

Ce^{4+}/Ce^{3+} ratios are calculated by the method of Ballard et al. (2002).

the Cu-mineralized and non-mineralized plutons may be attributed to different magmatic sources, which is traced by whole-rock Sr and Nd isotopes of these four plutons. Previous studies showed that the Pulang pluton had higher whole-rock εNd(t) values (−0.62 to 2.12) than those of the Cuojiaoma and Dongcuo plutons (−9.5 to − 6.2). However, the former pluton did not show lower $(^{87}Sr/^{86}Sr)_i$ ratios (0.7052 to 0.7102) than those of the latter plutons (0.7080–0.7095) (Wang et al., 2018; Wu et al., 2017). In general, this decoupling of Sr and Nd isotopes characteristics may result from post-magmatic metasomatic processes (e.g., Liu et al., 2015). More evidence is therefore needed to trace magmatic sources. The apatite Nd isotope is a reliable reflection for the initial magmatic Nd isotope signature because the early crystallization of apatite considerably avoided the isotope fractionation due to the crystallization of other mineral phases. Our data show that the apatites from the Pulang pluton have higher εNd(t) values than those from the other three plutons (see Fig. 10). This finding, together with the whole-rock Nd isotopes, indicates that the parental magma of the Pulang pluton was derived from a source that comprised more mantle-derived components.

In addition, on the basis of chemical characteristics, the Cu-mineralized Pulang pluton shows adakitic affinity, whereas the non Cu-mineralized plutons (Cuojiaoma, Dongcuo, and Daocheng) cannot. The apatite crystals from the Pulang pluton show higher values of Sr/Y, La/Yb, and δEu than those from the other three plutons (see Fig. 11). This matches the whole-rock compositional variations and indicates that these chemical compositions in apatite can be used to identify adakite-like rocks. This finding is significant, especially considering that highly altered or weathered rocks cannot preserve the original value of Sr/Y, La/Yb, and δEu. Moreover, apatite is not susceptible to alteration as feldspar that is the main sink of whole-rock Sr and Eu.

The adakitic intrusive suites might have been derived from slab melts that interacted with the overlying metasomatized mantle wedge (Wang et al., 2011). Since the subducted Garzê-Litang Ocean is regarded as well-aerated and not anoxic as the Paleo-Tethys Ocean basin (Richards, 2015b), this causative magma of the Pulang pluton can thus be oxidized. Alternatively, there is a popular view attributing the adakitic affinity of Cu-mineralized porphyries to high magmatic water contents (> 10 wt%) (Lu et al., 2015), which induces early amphibole fractionation (depletion of Y and Yb in melt) and suppression of plagioclase crystallization (increase of Sr and Eu in melt) (Richards, 2011; Loucks, 2014). Correspondingly, the adakitic porphyries typically have Sr/Y > 40 and Eu/Eu* close to one, and zircon Eu/Eu* > 0.4 (Lu et al., 2016, 2019). The high water content can also explain the high magmatic oxygen fugacity and Cl abundance because both H_2O and Cl are similarly incompatible, and will increase in concentration in the melt during magma fractionation. Consistent with these understandings, a recent study revealed that the Pulang pluton was indeed formed by a highly hydrous magma (Li et al., 2019). However, the Cuojiama, Dongcuo and Daocheng plutons were generated by the partial melting of the Late Paleoproterozoic-Early Mesoproterozoic lower crust (Qu et al., 2002, He et al., 2013). The lack of the modification of magma source by slab melts and fluids results in these non-adakitic magmas to be reduced and being infertile for the porphyry-type Cu mineralization.

The reason why the distribution of the fertile adakitic rocks is concentrated in the southern part of the Yidun Arc belt rather than the north of it is still enigmatic. There is a possible explanation from the studies of Hou et al. (2001); (2004; 2007;)). These authors proposed that the Garzê-Litang Oceanic lithosphere subducted westward at a steep angle in the northern Yidun Arc belt, forming a tensional arc that is conducive to the formation of VMS-type Pb-Zn deposit rather than porphyry-type Cu deposit. However, the oceanic lithosphere subducted at a shallow to flat angle in the southern Yidun Arc belt, thereby resulting in a compressional arc and triggering several adakite-like rocks and related porphyry Cu deposits. It is difficult to appraise this hypothesis through our study. But the significant differences in magmatic sources and compositions of the four coeval granitoids, which is

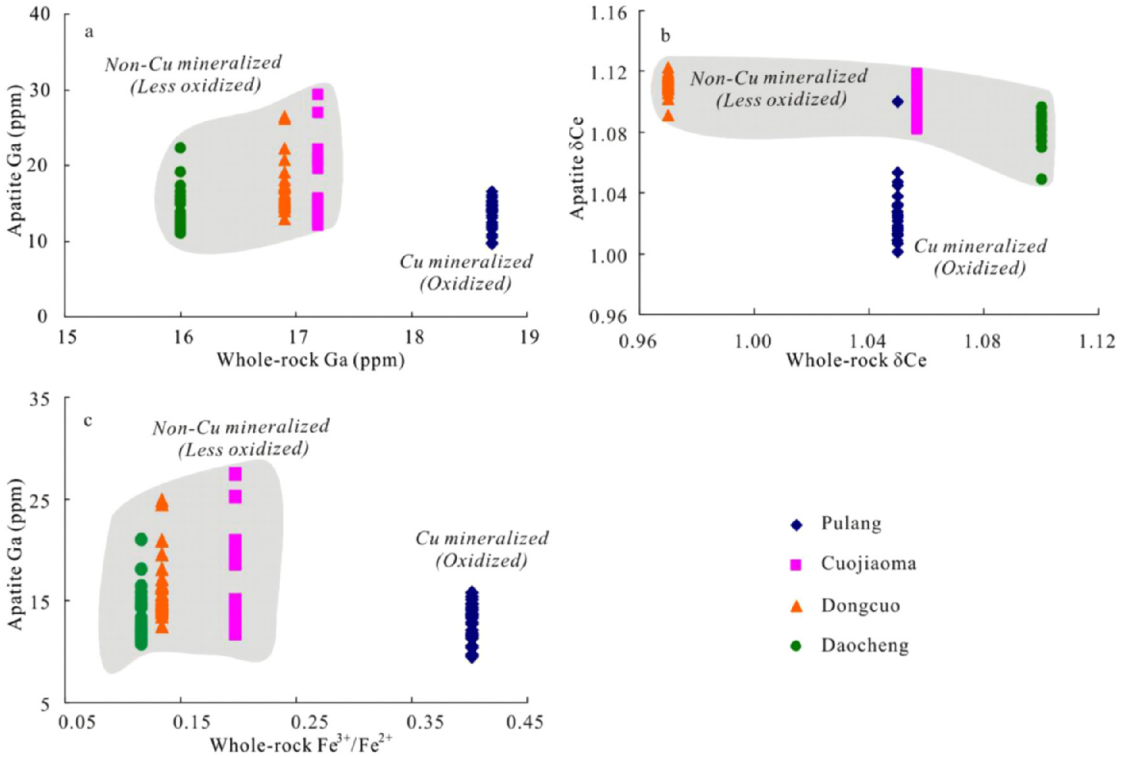

Fig. 8. Plots of whole-rock Ga versus apatite Ga (a), whole-rock δCe versus apatite δCe (b), and whole-rock Fe^{3+}/Fe^{2+} ratio versus apatite Ga (c).

revealed by apatite chemical composition, perhaps suggest the different tectonic settings in which these granitoids were formed.

5.4. Implications for porphyry Cu mineralization in the Yidun Arc belt

Traditionally, porphyry Cu deposits are considered to have formed by magmas that were oxidized and unusually rich in Cu (e.g., Halter et al., 2006; Core et al., 2006; Stern et al., 2007; Richards, 2015a). But

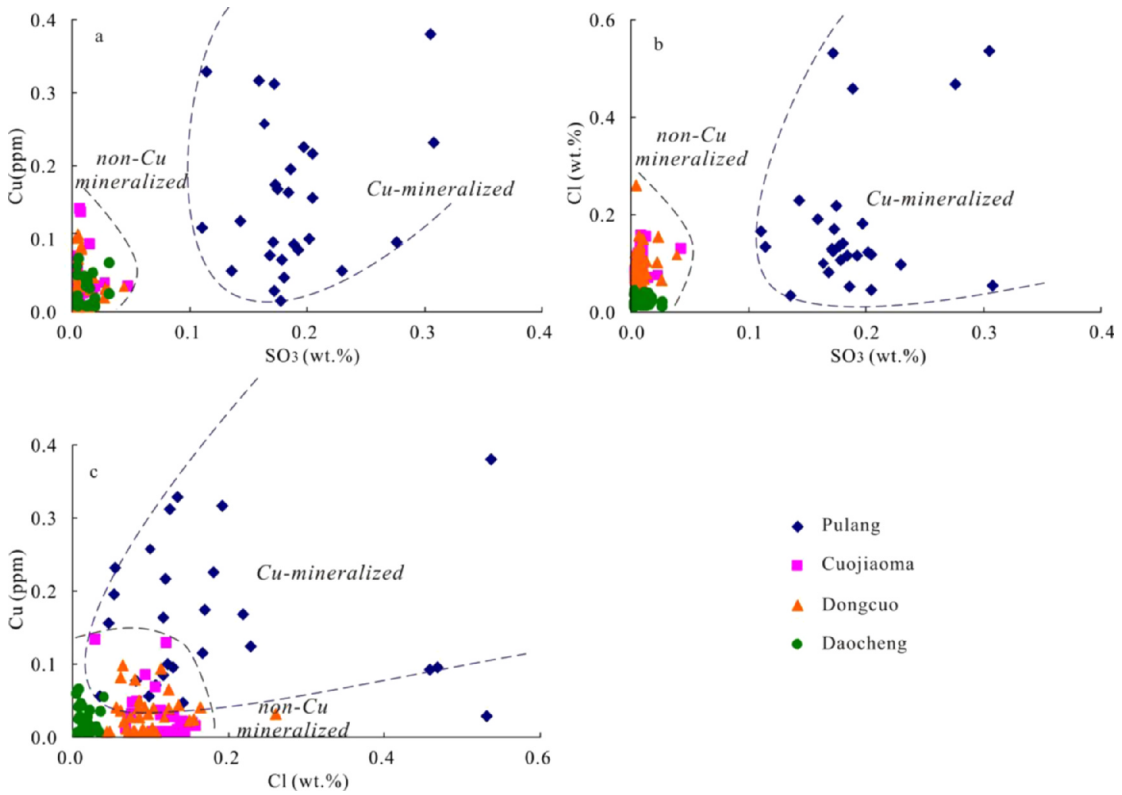

Fig. 9. Plots of SO_3 versus Cu (a), SO_3 versus Cl (b), and Cl versus Cu (c) in the apatites from the selected plutons.

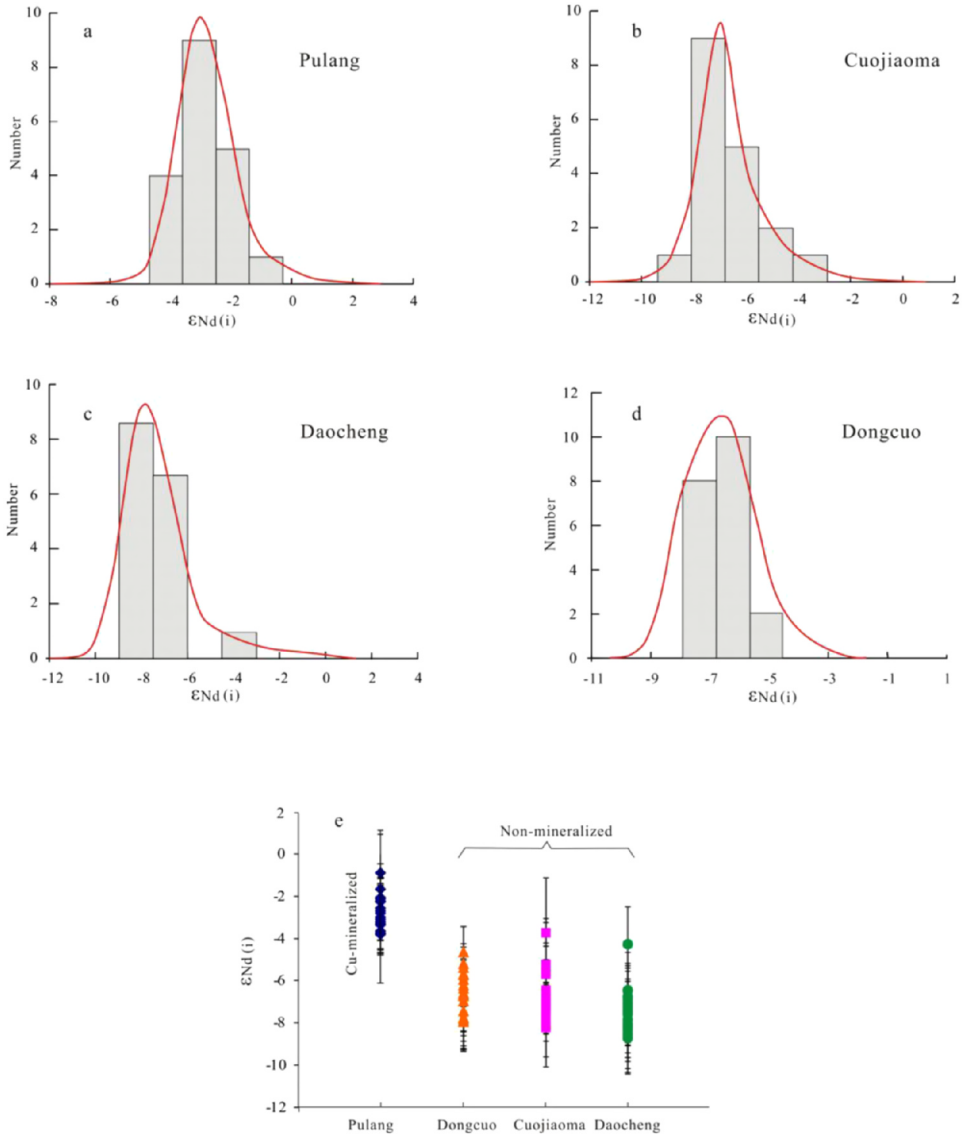

Fig. 10. Probability density plot of apatite εNd(i) values in the Pulang (a), Cuojiaoma (b), Dongcuo (c) and Daocheng (d) plutons, and the variation of apatite εNd(i) values in these four plutons (e).

some recent studies suggested that this view may not be entirely true. For example, Xu et al. (2019) found that the parental magma of the Cu-mineralized plutons (e.g. Tongchang) that located in the western rim of the South China block, are less oxidized than that of the coeval non-mineralized plutons (e.g. Shilicun). Moreover, the study on the melt and sulfide inclusions at the Bingham Canyon latite (Zhang and Audétat, 2017) indicated that through highly efficient extraction of Cu, the magmas without unusually high Cu concentration can also generate porphyry Cu deposits. Such findings suggest that the roles of magmatic oxidation state and Cu concentration in porphyry Cu mineralization may not be as important as traditionally thought. Despite these above controversies, the results from our study have shown that the parental magma of the Cu-mineralized Pulang pluton is indeed more fertile than that of the other three non-mineralized plutons. This observation means that although the potential of porphyry Cu mineralization of the magmas that do not have unusually high Cu concentration and high oxygen fugacity cannot be underestimated, the Cu-rich and oxidized magmas could have more opportunities for porphyry Cu mineralization than the formers, at least for the felsic magmas in the Yidun Arc belt, eastern Tibet.

6. Conclusions

1) The abundances of Ga, S, Cu and Cl and δCe value of apatite and zircon Ce^{4+}/Ce^{3+} ratio indicate the parental magma of the Cu-mineralized Pulang pluton is more oxidized and richer in Cu, S and Cl than that of the non-mineralized Cuojiaoma, Dongcuo and Daocheng plutons.
2) The aforementioned differences in magmas can be ascribed to the different magma sources and natures of these four plutons. Apatite δEu, Sr/Y, and La/Yb and Nd isotope show that the parental magma of the Pulang pluton is adakitic and contains more mantle components than that of the other three plutons.
3) The difference in magmatic fertility is a crucial factor for different Cu-mineralization potential of the Paleo-Tethyan granitoids in the eastern Tibet. Apatite as an effective tool for tracing magmatic fertility could have great potential application in porphyry magmatic metallogenic system.

Declaration of Competing Interest

The authors declare that they have no known competing financial

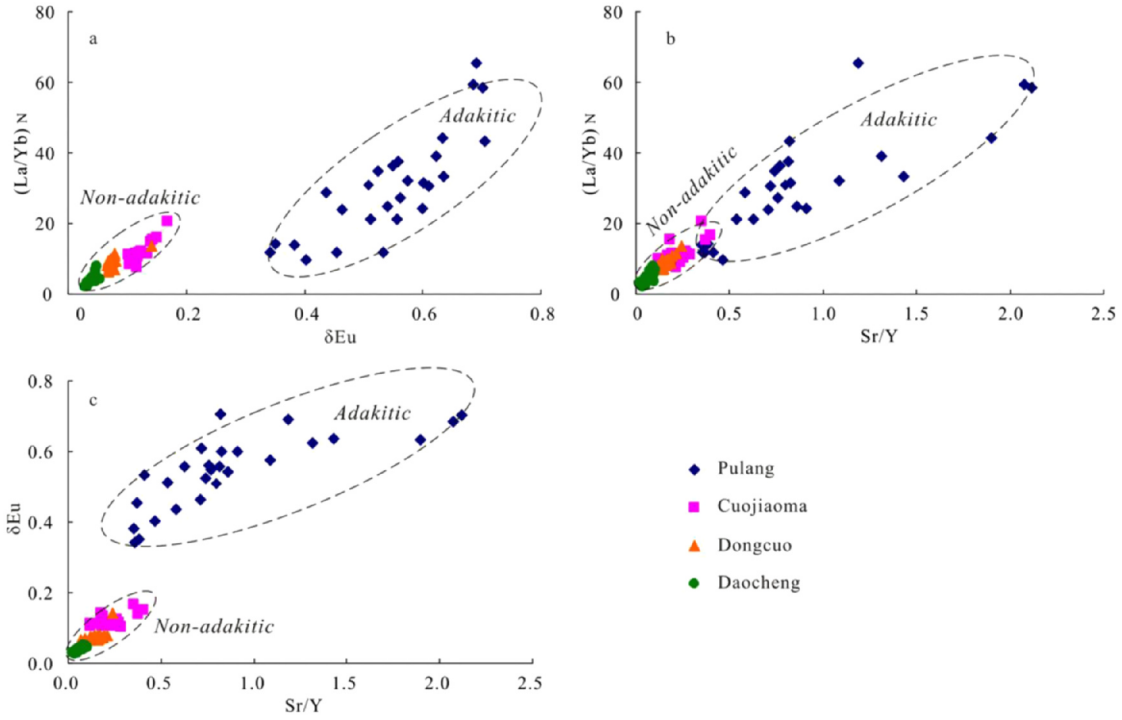

Fig. 11. Plots of δEu versus $(La/Yb)_N$ (a), Sr/Y versus $(La/Yb)_N$ (b), and Sr/Y versus δEu (c) in the apatites from the selected plutons.

interests or personal relationships that could have appeared to influence the work reported in this paper.

Acknowledgments

This study was supported by the National Natural Science Foundation of China (Grant 41703050), the Strategic Priority Research Program (B) of the Chinese Academy of Sciences (XDB18000000) and "Light of West China" Program of Chinese Academy of Sciences. We thank Yan-Wen Tang for his assistance in apatite and zircon trace element analysis by LA-ICP-MS, Wen-Qin Zheng and Xiang Li for their support in apatite chemical analysis by EPMA, You-Wei Chen for his help in apatite Nd isotope analysis by LA-MC-ICP-MS and Jing Hu and Shu-Qin Yang for their assistance in the whole-rock chemical analysis by XRF and ICP-MS. Dr. Jing-Jing Zhu and Ming-liang Huang are thanked for discussion with them giving us lots of ideas.

Appendix A. Supplementary data

Supplementary data to this article can be found online at https://doi.org/10.1016/j.oregeorev.2020.103757.

References

Ayers, J.C., Watson, E.B., 1991. Solubility of apatite, monazite, zircon, and rutile in supercritical aqueous fluids with implications for subduction zone geochemistry. Philos. Trans. R Soc. London, Ser. A335, 365–375.
Ballard, J.R., Palin, J.M., Campbell, I.H., 2002. Relative oxidation states of magmas inferred from Ce(IV)/Ce(III) in zircon: application to porphyry copper deposits of Northern Chile. Contrib. Mineral. Petr. 144, 347–364.
Belousova, E.A., Griffin, W.L., O'Reilly, S.Y., Fisher, N.I., 2002. Apatite as an indicator mineral for mineral exploration: trace-element composition and their relationship to host rock type. J. Geochem. Explor. 76, 45–69.
Bi, X.W., Cornell, D.H., Hu, R.Z., 2002. REE composition of primary and altered feldspar from the mineralized alteration zone of alkali-rich intrusive rocks, Western Yunnan Province, China. Ore Geol. Rev. 19, 69–78.
Boudreau, A.E., McCallum, I.S., 1989. Investigations of the stillwater complex: part V. Apatites as indicators of evolving fluid composition. Contrib. Mineral. Petr. 102, 138–153.
Boudreau, A.E., Kruger, F.J., 1990. Variation in the composition of apatite through the Merensky cyclic unit in the Western Bushveld Complex. Econ. Geol. 85, 737–745.
Bouzari, F., Hart, C.J.R., Bissig, T., Barker, S., 2016. Hydrothermal alteration revealed by apatite luminescence and chemistry: a potential indicator mineral for exploring covered porphyry copper deposits. Econ. Geol. 111, 1397–1410.
Candela, P.A., Holland, H.D., 1984. The partitioning of copper and molybdenum between silicate melts and aqueous fluids. Geochim. Cosmochim. Ac. 48, 373–388.
Candela, P.A., 1986. Toward a thermodynamic model for the halogens in magmatic systems: an application to melt-vapor-apatite equilibria. Chem. Geol. 57, 289–301.
Cao, K., Yang, Z.M., Xu, J.F., Fu, B., Li, W.K., Sun, M.Y., 2018. Origin of dioritic magma and its contribution to porphyry Cu-Au mineralization at Pulang in the Yidun arc, eastern Tibet. Lithos 304–307, 436–449.
Cao, K., Yang, Z.M., Mavrogenes, J., White, N.C., Xu, J.F., Li, Y., Li, W.K., 2019. Geology and genesis of the giant Pulang porphyry Cu-Au district, Yunnan, Southwest China. Econ. Geol. 114, 275–301.
Cao, M.J., Li, G.M., Qin, K.Z., Seitmuratova, E.Y., Liu, Y.S., 2012. Major and trace element characteristics of apatites in granitoids from Central Kazakhstan: implications for petrogenesis and mineralization. Resour. Geol. 62, 63–83.
Cline, J.S., Bodnar, R.J., 1991. Can economic porphyry copper mineralization be generated by a typical calc-alkaline melt? J. Geophys. Res. 96, 8113–8126.
Core, D.P., Kesler, S.E., Essene, E.J., 2006. Unusually Cu-rich magmas associated with giant porphyry copper deposits: evidence from Bingham, Utah. Geology 34, 41–44.
Creaser, R.A., Gray, C.M., 1992. Preserved initial $^{87}Sr/^{86}Sr$ in apatite from altered felsic igneous rocks: a case study from Middle Proterozoic of South Australia. Geochim. Cosmochim. Ac. 56, 2789–2795.
Harrison, T.M., Watson, E.B., 1984. The behavior of apatite during crustal anatexis: equilibrium and kinetic consideration. Geochim. Cosmochim. Ac. 48, 1467–1477.
Halter, W.E., Heinrich, C.A., Pettke, T., 2006. Magma evolution and the formation of porphyry Cu-Au ore fluids: evidence from silicate and sulfide melt inclusions. Miner. Deposita. 39, 845–863.
He, D.F., Zhu, W.G., Zhong, H., Ren, T., Bai, Z.J., Fan, H.P., 2013. Zircon U-Pb geochronology and elemental and Sr–Nd–Hf isotopic geochemistry of the Daocheng granitic pluton from the Yidun Arc, SW China. J. Asian Earth Sci. 67–68, 1–13.
Hou, Z.Q., Yang, Y.Q., Qu, X.M., Huang, D.H., Lv, Q.T., Wang, H.P., Yu, J.J., Tang, S.H., 2004. Tectonic evolution and mineralization systems of the Yidun arc orogen in Sanjiang region, China. Acta. Geol. Sin. 78, 109–120 (in Chinese with English abstract).
Hou, Z.Q., Qu, X.M., Zhou, J.R., Yang, Y.Q., Huang, D.H., Lv, Q.T., Tang, S.H., Yu, J.J., Wang, H.P., Zhao, J.H., 2001. Collision-orogenic processes of the Yidun arc in the Sanjiang region: record of granites (in Chinese with English abstract). Acta. Geol. Sin. 75, 484–497.
Hou, Z.Q., Yang, Y.Q., Wang, H.P., Qu, X.M., Lü, Q.T., Huang, D.H., Wu, X.Z., Yu, J.J., Tang, S.H., Zhao, J.H., 2003. The collisional orogeny and mineralization systems of the Yidun Arc orogen in Sanjiang region, China. Geological Publishing House, Beijing 154–187 (in Chinese with English abstract).
Hou, Z.Q., Zaw, K., Pan, G.T., Mo, X.X., Xu, Q., Hu, Y.Z., Li, X.Z., 2007. Sanjiang tethyan metallogenesis in SW China: tectonic setting, metallogenic epochs and deposit types. Ore Geol. Rev. 31, 48–87.
Imai, A., 2002. Metallogenesis of porphyry Cu deposits of the western Luzon arc, Philippines: K-Ar ages, SO_3 contents of microphenocrystic apatite and significance of intrusive rocks. Resour. Geol. 52, 147–161.

Imai, A., 2004. Variation of Cl and SO3 contents of microphenocrystic apatite in intermediate to silicic igneous rocks of Cenozoic Japanese island arcs: implications for porphyry Cu metallogenesis in the Western Pacific Island arcs. Resour. Geol. 54, 357–372.
Isnard, H., Brennetot, R., Caussignac, C., Caussignac, N., Chartier, F., 2005. Investigations for determination of Gd and Sm isotopic compositions in spent nuclear fuels samples by MC ICPMS. Int. J. Mass Spectrom. 246, 66–73.
Lai, Q.Z., Ding, L., Wang, H.W., Yue, Y.H., Cai, F.L., 2007. Constraining the stepwise migration of the eastern Tibetan Plateau margin by apatite fission track thermochronology. Sci. China Ser. D 50, 172–183.
Leng, C.B., Gao, J.F., Chen, W.T., Zhang, X.C., Tian, Z.D., Guo, J.H., 2018a. Platinum-group elements, zircon Hf-O isotopes, and mineralogical constraints on magmatic evolution of the Pulang porphyry Cu-Au system, SW China. Gondwana Res. 62, 163–177.
Leng, C.B., Cooke, D.R., Hou, Z.Q., Evans, N.J., Zhang, X.C., Chen, W.T., Danišík, M., McInnes, B.I.A., Yang, J.H., 2018b. Quantifying exhumation at the giant Pulang porphyry Cu-Au deposit using U-Pb-He dating. Econ. Geol. 113, 1077–1092.
Li, W.C., Zeng, P.S., Hou, Z.Q., White, N.C., 2011. The Pulang porphyry copper deposit and associated felsic intrusions in Yunnan Province, southwest China. Econ. Geol. 106, 79–92.
Li, W.K., Yang, Z.M., Cao, K., Lu, Y.J., Sun, M.Y., 2019. Redox-controlled generation of the giant porphyry Cu-Au deposit at Pulang, southwest China. Contrib. Mineral. Petr. 174. https://doi.org/10.1007/s00410-019-1546-x.
Liu, S.W., Wang, Z.Q., Yan, Q.R., Li, Q.G., Zhang, D.H., 2006. Indosinian tectonic setting of the Southern Yidun Arc: constraints from SHRIMP zircon chronology and geochemistry of dioritic porphyries and granites. Acta. Geol. Sin.-Engl. 80, 387–399.
Liu, H., Wang, Q.F., Zhang, C.Q., Lou, D.B., Zhou, Y.M., He, Z.H., 2016. Spatial pattern and dynamic control for mineralization in the Pulang porphyry copper deposit, Yunnan, SW China: perspective from fractal analysis. J. Geochem. Explor. 164, 42–53.
Liu, Y.H., Yang, H.J., Takazawa, E., Satish-Kumar, M., You, C.F., 2015. Decoupling of the Lu-Hf, Sm-Nd, and Rb-Sr isotope systems in eclogites and a garnetite from the Sulu ultra-high pressure metamorphic terrane: causes and implications. Lithos 234–235, 1–14.
Liu, Y.S., Hu, Z.C., Gao, S., Gunther, D., Xu, J., Gao, C.G., Chen, H.H., 2008. In situ analysis of major and trace elements of anhydrous minerals by LA-ICP-MS without applying an internal standard. Chem. Geol. 257, 34–43.
Loucks, R.R., 2014. Distinctive composition of copper-ore-forming arc magmas. Aust J. Earth Sci. 61, 5–16.
Lu, Y.J., Loucks, R.R., Fiorentini, M.L., Yang, Z.M., Hou, Z.Q., 2015. Fluid flux melting generated post-collisional high-Sr/Y copper-ore-forming water-rich magmas in Tibet. Geology 43, 583–586.
Lu, Y.J., Loucks, R.R., Fiorentini, M.L., McCuaig, T.C., Evans, N., Yang, Z.M., Hou, Z.Q., Kirkland, C., Parra-Avila, L.A., Kobussen, A., 2016. Zircon compositions as a pathfinder for porphyry Cu ± Mo ± Au deposits. Society of Economic Geologists Special Publication 19, 329–347.
Lu, Y.J., Smithies, R.H., Wingate, M.T.D., Evans, N.J., McCuaig, T.C., Champion, D.C., Outhwaite, M., 2019. Zircon fingerprinting of magmatic-hydrothermal systems in the Archean Yilgarn Craton: Geological Survey of Western Australia, Report 197, 22 (freely available at http://dmpbookshop.eruditetechnologies.com.au/product/zircon-fingerprinting-of-magmatichydrothermal-systems-in-the-archean-yilgarn-craton.do).
Maniar, P.D., Piccoli, P.M., 1989. Tectonic discrimination of granitoids. Geol. Soc. Am. Bull. 101, 635.
Meurer, W.P., Boudreau, A.E., 1996. An evaluation of models of apatite compositional variability using apatite from the Middle Banded series of the Stillwater Complex, Montana. Contrib. Mineral. Petr. 125, 225–236.
Mo, X., Deng, J., Lu, F., 1994. Volcanism and the evolution of Tethys in Sanjiang area, southwestern China. J. SE Asian Earth Sci. 9, 325–333.
Palma, G., Barra, F., Reich, M., Valencia, V., Simon, A.C., Vervoort, J., Leisen, M., Romero, R., 2019. Halogens, trace element concentrations, and Sr-Nd isotopes in apatite from iron oxide-apatite (IOA) deposits in the Chilean iron belt: evidence for magmatic and hydrothermal stages of mineralization. Geochim. Cosmochim. Ac. 246, 515–540.
Pan, Y., Fleet, M.E., 2002. Compositions of the apatite group minerals: substitution mechanisms and controlling factors. Rev. Mineral Geochem. 48, 13–49.
Pang, Z.S., Du, Y.S., Wang, G.W., Gao, X., Li, Q., 2009. Single-grain zircon U-Pb isotopic ages, geochemisrty and its implication of the Pulang complex in Yunnan Province, China. Acta Petrol. Sin. 25, 159–165.
Pang, Z.S., Du, Y.S., Cao, Y., Gao, F.P., Wang, G.W., Dong, Q., 2014. Geochemistry and zircon U-Pb geochronology of the Pulang Complex, Yunnan Province. China. J. Earth Syst. Sci. 123, 875–885.
Peng, T.P., Zhao, G.C., Fan, W.M., Peng, B.X., Mao, Y.S., 2014. Zircon geochronology and Hf isotopes of Mesozoic intrusive rocks from the Yidun terrane, Eastern Tibetan Plateau: petrogenesis and their bearings with Cu mineralization. J. Asian Earth Sci. 80, 18–33.
Piccoli, P.M., Candela, P.A., 2002. Apatite in igneous systems. Rev. Mineral Geochem. 48, 255–292.
Qi, L., Hu, J., Gregoire, D.C., 2000. Determination of trace elements in granites by inductively coupled plasma mass spectrometry. Talanta 51, 507–513.
Qu, X.M., Hou, Z.Q., Zhou, S.G., 2002. Geochemical and Nd, Sr isotopic study of the postcollisional granites in the Yidun Arc belt of northern Sanjiang region, southwestern China. Resour. Geol. 52, 163–172.
Reid, A., Wilson, C.J.L., Shun, L., Pearson, N., Belousova, E., 2007. Mesozoic plutons of the Yidun Arc, SW China: U/Pb geochronology and Hf isotopic signature. Ore Geol. Rev. 31, 88–106.
Richards, 2011. High Sr/Y arc magmas and porphyry Cu ± Mo ± Au deposits: just add water. Econ Geol. 106, 1075–1081.
Richards, J.P., 2015a. The oxidation state, and sulfur and Cu contents of arc magmas: implications for metallogeny. Lithos 233, 27–45.
Richards, J.P., 2015b. Tectonic, magmatic, and metallogenic evolution of the Tethyan orogen: from subduction to collision. Ore Geol. Rev. 70, 323–345.
Richards, J.P., Şengör, A.M.C., 2017. Did Paleo-Tethyan anoxia kill arc magma fertility for porphyry copper formation? Geol. Soc. Am. Bull 45, 591–594.
Roger, F., Jolivet, M., Malavieille, J., 2008. Tectonic evolution of the Triassic fold belts of Tibet. Cr. Geosci. 340, 180–189.
Roger, F., Jolivet, M., Malavieille, J., 2010. The tectonic evolution of the Songpan-Garz (North Tibet) and adjacent areas from Proterozoic to present: a synthesis. J. Asina. Earth. Sci. 39, 254–269.
RØnsbo, J.G., 1989. Coupled substitutions involving REEs and Na and Si in apatites in alkaline rocks from the Ilĺmaussaq intrusion, South Greenland, and the petrological implications. Am. Mineral. 74, 896–901.
Schisa, P., Boudreau, A., Djon, L., Tchalikian, A., Corkery, J., 2015. The Lac Des Iles Palladium Deposit, Ontario, Canada. Part II.Halogen variations in apatite. Miner Deposita 50, 339–355.
Seedorf, E., Dilles, J.H., Proffett, J.M., Einacdi, M.T., 2005. Porphyry deposits: characteristics and origin of hypogene features. Econ. Geol. 100, 251–298.
Sha, L.K., Chappell, B.W., 1999. Apatite chemical composition, determined by electron microprobe and laser-ablation inductively coupled plasma mass spectrometry, as a probe into granite petrogenesis. Geochim. Cosmochim. Ac. 63, 3861–3881.
Sillitoe, R.H., 2010. Porphyry copper systems. Econ. Geol. 105, 3–41.
Song, X.Y., Zhou, M.F., Cao, Z.M., Robinson, P.T., 2004. Late Permian rifting of the South China Craton caused by the Emeishan mantle plume? J. Geol. Soc. London 161, 773–781.
Stern, C.R., Funk, J.A., Skewes, M.A., Arévalo, A., 2007. Magmatic anhydrite in plutonic rocks at the El Teniente Cu-Mo deposit, Chile, and the role of sulfur-and copper-rich magmas in its formation. Econ. Geol. 102, 1335–1344.
Sun, S.J., Yang, X.Y., Wang, G.J., Sun, W.D., Zhang, H., Li, C.Y., Ding, X., 2019. In situ elemental and Sr-O isotopic studies on apatite from the Xu-Huai intrusion at the southern margin of the North China Craton: Implications for petrogenesis and metallogeny. Chem. Geol. 510, 200–214.
Sun, S.S., McDonough, W.F., 1989. Chemical and isotopic systematics of oceanic basalts: implications for mantle composition and processes. Geological Society Special Publication 42, 313–345.
Tepper, J.H., Kuehner, S.M., 1999. Complex zoning in apatite from the Idaho batholith: a record of magma mixing and intracrystalline trace element diffusion. Am. Mineral. 84, 581–595.
Wang, B.Q., Zhou, M.F., Li, J.W., Yan, D.P., 2011. Late Triassic porphyritic intrusions and associated volcanic rocks from the Shangri-La region, Yidun terrane, Eastern Tibetan Plateau: adakitic magmatism and porphyry copper mineralization. Lithos 127, 24–38.
Wang, B.Q., Zhou, M.F., Chen, W.T., Gao, J.F., Yan, D.P., 2013. Petrogenesis and tectonic implications of the Triassic volcanic rocks in the northern Yidun Terrane, Eastern Tibet. Lithos 175–176, 285–301.
Wang, H., Zhang, Y., Chu, Y., Ma, H., Li, Y., Wu, D., Du, B., Wei, Q., 2016. Disposable competitive-type immunoassay for determination of aflatoxin B1 via detection of copper ions released from Cu-apatite. Talanta 147, 556–560.
Wang, P., Dong, G.C., Dong, M.L., Li, Y.P., Xu, Y.M., Pan, Y.N., Chen, W., Wu, Z.C., 2017. Magma mixing of the Cuojiaoma batholith in the Yidun Arc: evidence from mafic microgranular enclaves Acta Petrol. Sin. 33, 2535–2547.
Wang, P., Dong, G.C., Zhao, G.C., Han, Y.G., Li, Y.P., 2018. Petrogenesis of the Pulang porphyry complex, southwestern China: implications for porphyry copper metallogenesis and subduction of the Paleo-Tethys Oceanic lithosphere. Lithos 304–307, 280–297.
Wang, X.S., Bi, X.W., Leng, C.B., Zhong, H., Tang, H.F., Chen, Y.W., Yin, G.H., Huang, D.Z., Zhou, M.F., 2014. Geochronology and geochemistry of Late Cretaceous igneous intrusions and Mo-Cu-(W) mineralization in the southern Yidun arc, SW China: implications for metallogenesis and geodynamic setting. Ore Geol. Rev. 61, 73–95.
Watson, E.B., 1979. Apatite saturation in basic to intermediate magmas. Geophys. Res. Lett. 6, 937–940.
Watson, E.B., 1980. Apatite and phosphorus in mantle source regions: an experimental study of apatite/melt equilibria at pressures to 25 kbar. Earth. Planet. Sc. Lett. 51, 322–335.
Webster, J.D., 2004. The exsolution of magmatic hydrosaline chloride liquids. Chem. Geol. 210, 33–48.
Weislogel, A.L., 2008. Tectonostratigraphic and geochronologic constraints on evolution of the northeast Paleotethys from the Songpan-Ganzi complex, central China. Tectonophysics 451, 331–345.
Williams-Jones, A.E., Candela, P.A., Piccoli, P.M., 1995. The partitioning of copper between silicate melts and two-phase aqueous fluids: an experimental investigation at 1 Kbar, 800°C and 0.5 Kbar, 850°C. Contrib. Mineral. Petr. 121, 388–399.
Wolf, M.B., London, D., 1994. Apatite dissolution into peraluminous haplogranite melt: an experimental study of solubilities and mechanisms. Geochim. Cosmochim. Ac. 58, 4127–4145.
Wu, T., Xiao, L., Wilde, S.A., Ma, C.Q., Zhou, J.X., 2017. A mixed source for the Late Triassic Garzê-Daocheng granitic belt and its implications for the tectonic evolution of the Yidun arc belt, eastern Tibetan Plateau. Lithos 288–289, 214–230.
Xiao, L., He, Q., Pirajno, F., Ni, P.Z., Du, J.X., Wei, Q.R., 2008. Possible correlation between a mantle plume and the evolution of Paleo-Tethys Jinshajiang Ocean: evidence from a volcanic rifted margin in the Xiaru-Tuoding area, Yunnan, SW China. Lithos 100, 112–126.
Xu, L.L., Bi, X.W., Hu, R.Z., Tang, Y.Y., Wang, X.S., Huang, M.L., Wang, Y.J., Ma, R., Liu, G., 2019. Contrasting whole-rock and mineral compositions of ore-bearing

(Tongchang) and ore-barren (Shilicun) granitic plutons in SW China: Implications for petrogenesis and ore genesis. Lithos 336–337, 54–66.
Yang, L.Q., Gao, X., Shu, Q.H., 2017. Multiple Mesozoic porphyry-skarn Cu (Mo-W) systems in Yidun Terrane, east Tethys: constraints from zircon U-Pb and molybdenite Re-Os geochronology. Ore Geol. Rev. 90, 813–826.
Yang, Q., Ren, Y.S., Chen, S.B., Zhang, G.L., Zeng, Q.H., Hao, Y.J., Li, J.M., Yang, Z.J., Sun, X.H., Sun, Z.M., 2019. Geological, Geochronological, and Geochemical Insights into the Formation of the Giant Pulang Porphyry Cu (–Mo–Au) Deposit in Northwestern Yunnan Province, SW China. Minerals 9. https://doi.org/10.3390/min9030191.
Yang, Y.H., Wu, F.Y., Yang, J.H., Chew, D.M., Xie, L.W., Chu, Z.Y., Huang, C., 2014. Sr and Nd isotopic compositions of apatite reference materials used in U-Th–Pb geochronology. Chem. Geol. 385, 35–55.
Zeng, P.S., Hou, Z.Q., Li, L.H., Qu, W.J., Wang, H.P., Li, W.C., Meng, Y.F., Yang, Z.S., 2004. Age of the Pulang porphyry copper deposit in NW Yunnan and its geological significance. Regional Geol. China 23, 1127–1131 (in Chinese with English abstract).
Zhang, D., Audétat, A., 2017. What caused the formation of the giant bingham canyon porphyry Cu-Mo-Au Deposit? Insights from melt inclusions and magmatic sulfides. Econ. Geol. 112, 221–244.